

Electron-phonon vertex correction effect in superconducting H₃S

Shashi B. Mishra,^{1,*} Hitoshi Mori,^{1,2} and Elena R. Margine^{1,†}

¹*Department of Physics, Applied Physics and Astronomy,
Binghamton University-SUNY, Binghamton, New York 13902, USA*

²*Institute for Materials Research, Tohoku University, Sendai 980-8577, Japan*

(Dated: July 16, 2025)

The Migdal-Eliashberg (ME) formalism provides a reliable framework for describing phonon-mediated superconductivity in the adiabatic regime, where the electronic Fermi energy exceeds the characteristic phonon energy. In this work, we go beyond this limit by incorporating first-order vertex corrections to the electron-phonon (e-ph) interaction within the Eliashberg formalism and assess their impact on the superconducting properties of H₃S and Pb using first-principles calculations. For H₃S, where the adiabatic assumption breaks down, we find that vertex corrections to the e-ph coupling are substantial. When combined with phonon anharmonicity and the energy dependence of the electronic density of states, the predicted critical temperature T_c is in very good agreement with experimental observations. In contrast, for elemental Pb, where the adiabatic approximation remains valid, vertex corrections have a negligible effect, and the calculated T_c and superconducting gap closely match the predictions of the standard ME formalism. These findings demonstrate the importance of non-adiabatic corrections in strongly coupled high- T_c hydrides and establish a robust first-principles framework for accurately predicting superconducting properties across different regimes.

I. INTRODUCTION

The Migdal-Eliashberg (ME) theory [1–3] is a powerful many-body method for predicting superconducting properties and is widely regarded as the standard theory for conventional phonon-mediated superconductivity [4–11]. The theory, as formulated by Eliashberg [2, 3], extends the weak-coupling limit of the Bardeen-Cooper-Schrieffer (BCS) model [12] by incorporating the Green's function approach developed by Migdal for describing the electron-phonon (e-ph) interaction in the normal metallic state [1]. Nowadays, first-principles simulations based on ME theory are performed routinely and at reasonable computational cost [13–15], showing good agreement with experiments across a wide range of conventional superconductors, from simple metals to complex materials [16–21].

Nevertheless, ME theory relies on Migdal's theorem [1], which assumes that the dynamics of electrons and ions happen on two well-separated energy scales, in accordance with the adiabatic Born-Oppenheimer approximation [22]. Migdal argued that vertex corrections to the bare e-ph scattering diagram can be neglected when the parameter $\lambda(\hbar\omega_0/\varepsilon_F)$ is small, where λ is the effective e-ph coupling constant, ω_0 is the characteristic phonon frequency, and ε_F is the Fermi energy. Specifically, it was shown that each additional term in the perturbative expansion of the e-ph vertex is suppressed by at least a factor of the order $\hbar\omega_0/\varepsilon_F \sim \sqrt{m/M} \sim 10^{-2}$, where m and M are the electron and ion mass. The condition $\lambda(\hbar\omega_0/\varepsilon_F) \ll 1$ is satisfied in most metallic systems since

the adiabatic parameter $\hbar\omega_0/\varepsilon_F \ll 0$, given that the electronic energy scale is of the order of several eV, whereas phonon energies are generally only a fraction of an eV.

However, the validity of Migdal's theorem has been called into question for several classes of superconductors such as superhydrides, fullerides, and systems with low charge carrier densities, where the electronic Fermi energy is small [23–34]. A natural generalization of the Eliashberg theory to the non-adiabatic regime can be achieved through a perturbative diagrammatic approach in the expansion parameter $\lambda(\hbar\omega_0/\varepsilon_F)$ [35–44]. This perturbative scheme is expected to remain applicable as long as λ is not larger than a critical value (of order 1) beyond which the system undergoes lattice transitions, leading to the formation of charge-density-waves or polaronic and/or bipolaronic states [44–47].

In recent years, there has been growing interest in understanding the impact of higher-order e-ph processes on key materials properties (e.g., spectral functions, band-gap renormalization, polaron formation, carrier mobility, or superconducting pairing) but studies that move beyond leading-order approximations remain rare [24, 32, 48–54]. This scarcity is primarily due to the rapid increase in computational complexity, as even incorporating second-order scattering events is highly nontrivial. Nonetheless, promising progress has been made, with several recent studies achieving such treatments fully from first principles [49–51]. On the superconductivity front, current approaches to non-adiabatic effects within the Eliashberg framework have relied on simplifying approximations. For example, in the anisotropic case, model Hamiltonians for the electronic structure, combined with an isotropic Einstein phonon spectrum and a single e-ph parameter, have been employed to solve the non-adiabatic Eliashberg equations [48]. In the isotropic case, besides replacing the momentum depen-

* mshashi125@gmail.com

† rmargine@binghamton.edu

dence in all kernels with Fermi-surface averages, further simplifications have been introduced, such as factorizing the lowest-order vertex correction kernel into a product of two e-ph interaction kernels [25, 48, 55].

In this work, we develop and implement a first-principles formalism to compute second-order e-ph vertex corrections within the isotropic Eliashberg framework [2, 3], extending beyond the conventional ME approximation [1, 8]. The main challenge in implementing this general treatment lies in the significantly increased computational cost, driven by two key factors. First, evaluating the vertex-corrected Eliashberg spectral function requires the computation of four distinct e-ph matrix elements associated with two phonons. Second, incorporating the resulting vertex-corrected e-ph interaction kernel into the Eliashberg equations introduces additional summations over Matsubara frequencies and integrations over electronic energies. Our methodology is implemented in the EPW code and supports both the full-bandwidth (FBW) and Fermi-surface restricted (FSR) approaches [56–58]. The FBW scheme retains the full energy dependence of the density of states (DOS), enabling the inclusion of e-ph scattering processes away from the Fermi level (ε_F), while FSR assumes a constant DOS near ε_F .

To demonstrate the capabilities of our non-adiabatic methodology, we investigate the effect of vertex corrections on the superconducting gap and critical temperature (T_c) of H_3S . This high- T_c superconductor serves as a prime example of a system where the adiabatic limit breaks down [23, 27]. At 200 GPa, a flat-band feature near ε_F gives rise to a van Hove singularities (vHs), leading to a small effective Fermi energy. Moreover, the characteristic phonon energy in H_3S exceeds 200 meV, yielding an adiabatic parameter of $\hbar\omega_0/\varepsilon_F \approx 5$ [27]. We find that the e-ph coupling constant with vertex corrections (λ^V) remains a significant fraction of the adiabatic coupling strength (λ), highlighting the persistence of strong coupling beyond the adiabatic regime in systems where the adiabatic limit breaks down, as is the case for many recently studied high- T_c hydrides [11, 27, 59].

Apart from vertex corrections, another critical factor in H_3S is the breakdown of the harmonic approximation, driven by hydrogen's low mass and significant quantum fluctuations [24, 60, 61]. These anharmonic effects renormalize phonon frequencies, particularly hydrogen-related modes, leading to strong phonon hardening and a consequent reduction in both the e-ph coupling and critical temperature. To examine the interplay between anharmonic and non-adiabatic effects, we compute the e-ph interactions and superconducting properties of H_3S by solving the Eliashberg equations in both the adiabatic and non-adiabatic regimes, with and without anharmonic phonons. Our results show that when both anharmonic and non-adiabatic effects are considered together, the resulting T_c falls within the experimental range.

Finally, we analyze the impact of vertex corrections in Pb, where the adiabatic limit is generally considered

valid. In this case, including vertex corrections results in a T_c nearly identical to that predicted within the adiabatic framework, confirming their negligible effect in systems where the Migdal approximation holds.

This paper is organized as follows. In Sec. II, we present the non-adiabatic Eliashberg theory and describe our *ab initio* implementation with lowest-order vertex corrections. Computational details and results for H_3S and Pb, both with and without vertex corrections, are provided in Secs. III and IV, respectively. Finally, Sec. V summarizes our findings. Additional details, including diagrammatic representation of e-ph self-energy, derivation of the isotropic non-adiabatic self-energy expression, symmetry reduction in the vertex-corrected spectral function, derivation of the isotropic non-adiabatic Eliashberg equations for both the FBW and FSR approaches, summation procedure over the Matsubara frequencies as well as convergence tests and additional results for H_3S with harmonic and anharmonic phonons, are included in the Supplementary Information [62].

II. THEORY

In this section, we review the theoretical background underlying phonon-mediated superconductivity, focusing on ME formalism and its extension to include the lowest-order vertex corrections. To solve the Eliashberg equations, we employ the FBW approach, which accounts for the full energy dependence of the electronic DOS. This is essential for accurately capturing the effects of sharp structures in the DOS, such as vHs, and allows for calculations with both fixed and self-consistently updated chemical potential (μ_F). We also present simplified expressions based on the constant DOS FSR approach.

A. Electron self-energy with electron-phonon vertex corrections

Within the Nambu formalism [63], the Hamiltonian of an electron-phonon interacting system can be written as

$$\hat{H} = \hat{H}_e + \hat{H}_{ph} + \hat{H}_{e-e} + \hat{H}_{e-ph}, \quad (1)$$

where

$$\hat{H}_e = \sum_{n\mathbf{k}} \varepsilon_{n\mathbf{k}} \hat{\Psi}_{n\mathbf{k}}^\dagger \hat{\tau}_3 \hat{\Psi}_{n\mathbf{k}} \quad (2)$$

$$\hat{H}_{ph} = \sum_{\mathbf{q}\nu} \hbar\omega_{\mathbf{q}\nu} \left(\hat{a}_{\mathbf{q}\nu}^\dagger \hat{a}_{\mathbf{q}\nu} + \frac{1}{2} \right) \quad (3)$$

$$\hat{H}_{e-e} = \frac{1}{2} \sum_{nm} \sum_{\mathbf{k}\mathbf{k}'} W_{n\mathbf{k}, m\mathbf{k}'} \left(\hat{\Psi}_{n\mathbf{k}'}^\dagger \hat{\tau}_3 \hat{\Psi}_{n\mathbf{k}} \right) \left(\hat{\Psi}_{m-\mathbf{k}'}^\dagger \hat{\tau}_3 \hat{\Psi}_{m-\mathbf{k}} \right) \quad (4)$$

$$\hat{H}_{e-ph} = \frac{1}{\sqrt{N_p}} \sum_{nm\nu} \sum_{\mathbf{k}\mathbf{q}} g_{m\mathbf{k}+\mathbf{q}, n\mathbf{k}}^{\mathbf{q}\nu} \left(\hat{a}_{\mathbf{q}\nu} + \hat{a}_{-\mathbf{q}\nu}^\dagger \right) \hat{\Psi}_{m\mathbf{k}+\mathbf{q}}^\dagger \hat{\tau}_3 \hat{\Psi}_{n\mathbf{k}}. \quad (5)$$

Here, $\hat{\tau}_i$ ($i = 0, 1, 2, 3$) are the Pauli matrices. Each of the terms is described below.

The first term represents the electron Hamiltonian, where $\hat{\Psi}_{n\mathbf{k}}$ is a two-component electron field operator

$$\hat{\Psi}_{n\mathbf{k}} = \begin{pmatrix} \hat{c}_{n\mathbf{k}\uparrow} \\ \hat{c}_{n-\mathbf{k}\downarrow}^\dagger \end{pmatrix}, \quad \hat{\Psi}_{n\mathbf{k}}^\dagger = \begin{pmatrix} \hat{c}_{n\mathbf{k}\uparrow}^\dagger & \hat{c}_{n-\mathbf{k}\downarrow} \end{pmatrix}, \quad (6)$$

with $\hat{c}_{n\mathbf{k}\sigma}^\dagger$ and $\hat{c}_{n\mathbf{k}\sigma}$ are the creation and annihilation operators for an electronic state with momentum \mathbf{k} , band index n , spin σ , and energy $\varepsilon_{n\mathbf{k}}$. The second term describes the phonon Hamiltonian, where $\omega_{\mathbf{q}\nu}$ is the frequency of a phonon mode with momentum \mathbf{q} and branch index ν , and $a_{\mathbf{q}\nu}^\dagger$ and $a_{\mathbf{q}\nu}$ are the bosonic creation and annihilation operators. The anharmonic terms, when relevant, are incorporated into Eq. (3) through additional contributions derived from the self-consistent phonon theory, which replaces the true double-well potential with an effective temperature-dependent harmonic potential that minimizes the free energy, as discussed in detail in Ref. [64]. The third term accounts for the Coulomb contribution, where $W_{n\mathbf{k},m\mathbf{k}+\mathbf{q}}$ are the scattering matrix elements between electrons.

The fourth term describes the e-ph interaction, as illustrated in Fig. 1(a), where N_p denotes the number of unit cells in the Born-von Kármán (BvK) supercell. This term corresponds to the conventional linear coupling between an electron and a phonon, commonly referred to as the Fan-Migdal term. Higher-order contributions to \hat{H}_{e-ph} , known as nonlinear e-ph interactions, could also influence materials properties [50–54, 65, 66], but are not considered in this work. The linear e-ph interaction term is governed by the matrix element $g_{m\mathbf{k}+\mathbf{q},n\mathbf{k}}^{\mathbf{q}\nu}$, which quantifies the scattering between electronic states $n\mathbf{k}$ and $m\mathbf{k}+\mathbf{q}$ mediated by a phonon with wavevector \mathbf{q} and branch index ν . This matrix element is defined as [67, 68]

$$g_{m\mathbf{k}+\mathbf{q},n\mathbf{k}}^{\mathbf{q}\nu} = \langle u_{m\mathbf{k}+\mathbf{q}} | \Delta_{\mathbf{q}\nu} v^{\text{KS}} | u_{n\mathbf{k}} \rangle_{\text{uc}}, \quad (7)$$

where $u_{n\mathbf{k}}$ is the Bloch-periodic part of the Kohn-Sham (KS) electron wavefunction, and the integral is performed over the unit cell (uc). The derivative of the self-consistent potential is given by

$$\Delta_{\mathbf{q}\nu} v^{\text{KS}} \equiv e^{-i\mathbf{q}\cdot\mathbf{r}} \Delta_{\mathbf{q}\nu} V^{\text{KS}} \\ = \sum_{\kappa\alpha\mathbf{R}_p} e^{-i\mathbf{q}\cdot(\mathbf{r}-\mathbf{R}_p)} \sqrt{\frac{\hbar}{2M_\kappa\omega_{\mathbf{q}\nu}}} e_{\kappa\alpha,\nu}(\mathbf{q}) \frac{\partial V^{\text{KS}}(\mathbf{r})}{\partial \tau_{\kappa\alpha p}}. \quad (8)$$

Here, κ labels atoms in the unit cell with M_κ as the atomic mass, and α denotes Cartesian directions. The index p labels unit cells with BvK boundary conditions, $\tau_{\kappa\alpha p}$ is the position of atom κ in the unit cell p , \mathbf{R}_p is the lattice vector identifying the unit cell p , and $e_{\kappa\alpha,\nu}(\mathbf{q})$ is the eigenvector corresponding to atom κ in the Cartesian direction α for a collective phonon mode $\mathbf{q}\nu$. The differential $\partial V^{\text{KS}}(\mathbf{r})/\partial \tau_{\kappa\alpha p}$ is computed using density functional perturbation theory (DFPT) [69]. In the presence of anharmonicity, the phonon modes are no longer exact eigenmodes of a harmonic potential, making $\Delta_{\mathbf{q}\nu} v^{\text{KS}}$

formally ill-defined. To incorporate anharmonic effects within Eq. (8), we retain the harmonic DFPT-computed potential derivatives while replacing the phonon eigenvectors and frequencies with their anharmonically renormalized counterparts, obtained by diagonalizing the dynamical matrix obtained from the special displacement method [64].

Using Nambu's notation, we define the finite-temperature electron Green's function as a 2×2 matrix [63]:

$$\hat{G}_{n\mathbf{k}}(\tau) = -\langle \hat{T}_\tau \hat{\Psi}_{n\mathbf{k}}(\tau) \hat{\Psi}_{n\mathbf{k}}^\dagger(0) \rangle \\ = -\begin{pmatrix} \langle \hat{T}_\tau \hat{c}_{n\mathbf{k}\uparrow}(\tau) \hat{c}_{n\mathbf{k}\uparrow}^\dagger(0) \rangle & \langle \hat{T}_\tau \hat{c}_{n\mathbf{k}\uparrow}(\tau) \hat{c}_{n-\mathbf{k}\downarrow}(0) \rangle \\ \langle \hat{T}_\tau \hat{c}_{n-\mathbf{k}\downarrow}^\dagger(\tau) \hat{c}_{n\mathbf{k}\uparrow}^\dagger(0) \rangle & \langle \hat{T}_\tau \hat{c}_{n-\mathbf{k}\downarrow}^\dagger(\tau) \hat{c}_{n-\mathbf{k}\downarrow}(0) \rangle \end{pmatrix}, \quad (9)$$

where \hat{T}_τ denotes Wick's time-ordering operator in imaginary time, and $\langle \dots \rangle$ indicates the grand-canonical thermodynamic average. The diagonal elements correspond to the normal Green's functions for spin-up and spin-down electrons, describing single-particle electronic excitations. The off-diagonal elements are the anomalous Green's functions, introduced by Gor'kov [70], which describe superconducting Cooper pairs. An important feature of the Nambu-Gor'kov formalism is that, in this matrix representation, the familiar Feynman-Dyson rules of many-body perturbation theory remain valid [71].

The study of the superconducting state involves the determination of the matrix Green's function in Eq. (9). In Matsubara space, this matrix Green's function obeys the Dyson equation [1, 72]:

$$[\hat{G}_{n\mathbf{k}}(i\omega_j)]^{-1} = [\hat{G}_{n\mathbf{k}}^0(i\omega_j)]^{-1} - \hat{\Sigma}_{n\mathbf{k}}(i\omega_j), \quad (10)$$

where $\hat{G}_{n\mathbf{k}}^0(i\omega_j)$ is the non-interacting Green's function

$$[\hat{G}_{n\mathbf{k}}^0(i\omega_j)]^{-1} = i\omega_j \hat{\tau}_0 - (\varepsilon_{n\mathbf{k}} - \mu_F) \hat{\tau}_3, \quad (11)$$

and $\hat{\Sigma}_{n\mathbf{k}}(i\omega_j)$ is the electron self-energy including contributions arising from the e-ph and Coulomb interactions

$$\hat{\Sigma}_{n\mathbf{k}}(i\omega_j) = \hat{\Sigma}_{n\mathbf{k}}^{\text{ep}}(i\omega_j) + \hat{\Sigma}_{n\mathbf{k}}^{\text{c}}(i\omega_j). \quad (12)$$

In these expressions, $i\omega_j = i(2j+1)\pi k_B T$ denotes the fermionic Matsubara frequency, where j is an integer, T is the temperature, and k_B is the Boltzmann constant.

Following the standard practice, the Coulomb part of the electron self-energy is defined within the GW approximation [73, 74] as

$$\hat{\Sigma}_{n\mathbf{k}}^{\text{c}}(i\omega_j) = -k_B T \sum_{m\mathbf{k}'} \sum_{j'} W_{n\mathbf{k},m\mathbf{k}'}(i\omega_j - i\omega_{j'}) \hat{\tau}_3 \hat{G}_{m\mathbf{k}'}(i\omega_{j'}) \hat{\tau}_3, \quad (13)$$

where $W_{n\mathbf{k},m\mathbf{k}'}(i\omega_j - i\omega_{j'})$ is the dynamically screened Coulomb interaction. Assuming a static screened Coulomb interaction, Eq. (13) simplifies to

$$\hat{\Sigma}_{n\mathbf{k}}^{\text{c}}(i\omega_j) = -k_B T \sum_{m\mathbf{k}'} \sum_{j'} W_{n\mathbf{k},m\mathbf{k}'} \hat{\tau}_3 \hat{G}_{m\mathbf{k}'}^{\text{od}}(i\omega_{j'}) \hat{\tau}_3, \quad (14)$$

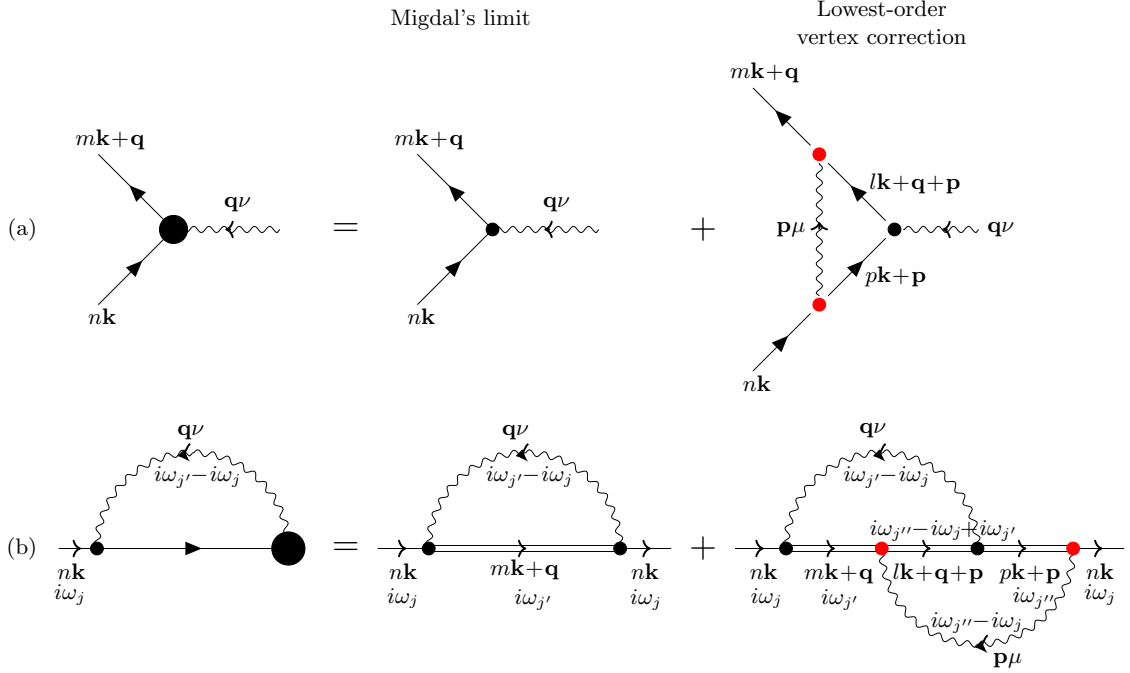


FIG. 1. First and second-order Feynman diagrams illustrating the (a) e-ph vertex and (b) the electron self-energy contributions arising from e-ph interactions. In these diagrams, straight lines represent bare electron Green's functions, straight double lines represent fully dressed electron Green's functions, and wavy lines denote bare phonon propagators. The second phonon-mediated e-ph vertex is indicated by red dots.

where only the off-diagonal components of the Green's function $\hat{G}_{n\mathbf{k}}^{\text{od}}(i\omega_j)$ are retained to avoid double counting Coulomb effects, since the one-particle eigenenergy $\varepsilon_{n\mathbf{k}}$ in $\hat{G}_{n\mathbf{k}}^0(i\omega_j)$ already includes part of the Coulomb interaction [8].

Recent methodological advancements have enabled a fully *ab initio* treatment of Coulomb interactions within Eliashberg theory [17–19, 75–77]. However, explicitly incorporating the full Coulomb kernel $W_{n\mathbf{k}, m\mathbf{k}'}$ in Eq. (14) remains computationally challenging. As a result, this interaction is typically approximated using the semi-empirical Morel-Anderson μ_c^* parameter [5, 78], defined as

$$\mu_c^* = \frac{\mu_c}{1 + \mu_c \ln \left(\frac{\varepsilon_{el}}{\hbar\omega_0} \right)}, \quad (15)$$

where μ_c is the Fermi-surface averaged Coulomb interaction, ω_0 is a characteristic phonon frequency, and ε_{el} is the electronic bandwidth. Within the Eliashberg formalism, the corresponding phonon energy scale is given by the Matsubara frequency cutoff ω_c , thus μ_c^* must be replaced by μ_E^* , which are related via [21, 79]

$$\frac{1}{\mu_E^*} = \frac{1}{\mu_c^*} + \ln \left(\frac{\omega_0}{\omega_c} \right). \quad (16)$$

This approximation is used in the current study.

For the phonon part, the central approximation consists of retaining only the first-order e-ph scattering diagram, shown in Fig. 1(b), for $\hat{\Sigma}_{n\mathbf{k}}^{\text{ep}}(i\omega_j)$, in line with

Migdal's theorem [1]. However, as discussed in Sec. I, this adiabatic approximation fails in several classes of superconductors, necessitating the inclusion of higher-order vertex corrections to the e-ph interaction [8, 39, 41, 42, 80], which forms the main focus of this work.

A detailed diagrammatic analysis, presented in Fig. S1 of the supplementary Information [62], demonstrates that next-order self-energy diagrams, such as the rainbow and parallel bubble diagrams, correspond to Fermi-surface-confined processes whose contributions are already implicitly accounted for in the Migdal approximation [8, 48, 81]. In contrast, the lowest-order vertex correction diagram in Fig. 1(b) captures non-adiabatic effects by involving intermediate electronic states that lie off-shell from the Fermi-surface, as illustrated in the corresponding scattering diagram shown in Fig. S1(h) [62]. In this work, we only include the lowest-order vertex correction. The explicit treatment of higher-order multi-phonon processes is deferred to future work, motivated by recent analytical toy model results indicating that the rainbow diagram can also influence the superconducting gap [52].

The electron self-energy $\hat{\Sigma}_{n\mathbf{k}}^{\text{ep}}(i\omega_j)$, incorporating both adiabatic (A) and non-adiabatic (NA) effects, is given by:

$$\hat{\Sigma}_{n\mathbf{k}}^{\text{ep}}(i\omega_j) = \Sigma_{n\mathbf{k}}^{(\text{A})}(i\omega_j) + \Sigma_{n\mathbf{k}}^{(\text{NA})}(i\omega_j). \quad (17)$$

The adiabatic self-energy $\hat{\Sigma}_{n\mathbf{k}}^{(\text{A})}(i\omega_j)$, corresponding to the

first-order Feynman diagram in Fig. 1, is expressed as

$$\hat{\Sigma}_{n\mathbf{k}}^{(A)}(i\omega_j) = -k_B T \sum_{m\mathbf{q}} \sum_{\nu j'} |g_{m\mathbf{k}+\mathbf{q},n\mathbf{k}}^{\mathbf{q}\nu}|^2 D_{\mathbf{q}\nu}(i\omega_j - i\omega_{j'}) \times \hat{\tau}_3 \hat{G}_{m\mathbf{k}+\mathbf{q}}(i\omega_{j'}) \hat{\tau}_3, \quad (18)$$

where $g_{m\mathbf{k}+\mathbf{q},n\mathbf{k}}^{\mathbf{q}\nu}$ is the screened e-ph coupling matrix element. Since \hat{H}_{e-ph} is Hermitian, the e-ph matrix element satisfy $g_{m\mathbf{k}+\mathbf{q},n\mathbf{k}}^{\mathbf{q}\nu} = [g_{n\mathbf{k},m\mathbf{k}+\mathbf{q}}^{-\mathbf{q}\nu}]^*$.

Following the standard practice [8], we replace the full phonon propagator $D_{\mathbf{q}\nu}(i\omega_j - i\omega_{j'})$ by the bare phonon Green's function

$$D_{\mathbf{q}\nu}^0(i\omega_j - i\omega_{j'}) = -\frac{2\omega_{\mathbf{q}\nu}}{(\omega_j - \omega_{j'})^2 + \omega_{\mathbf{q}\nu}^2}. \quad (19)$$

We define the anisotropic e-ph interaction kernel as

$$\lambda_{n\mathbf{k},m\mathbf{k}+\mathbf{q}}(i\omega_j - i\omega_{j'}) = \int_0^\infty d\omega \frac{2\omega}{(\omega_j - \omega_{j'})^2 + \omega^2} \times \alpha^2 F_{n\mathbf{k},m\mathbf{k}+\mathbf{q}}(\omega), \quad (20)$$

where the anisotropic Eliashberg spectral function is given by

$$\alpha^2 F_{n\mathbf{k},m\mathbf{k}+\mathbf{q}}(\omega) = N_F \sum_{\nu} |g_{m\mathbf{k}+\mathbf{q},n\mathbf{k}}^{\mathbf{q}\nu}|^2 \delta(\omega - \omega_{\mathbf{q}\nu}), \quad (21)$$

with N_F as the DOS per spin at ε_F . Substituting Eqs. (19)–(21) into the self-energy expression, Eq. (18) takes the compact form

$$\hat{\Sigma}_{n\mathbf{k}}^{(A)}(i\omega_j) = k_B T \sum_{m\mathbf{q}j'} \frac{\lambda_{n\mathbf{k},m\mathbf{k}+\mathbf{q}}(i\omega_j - i\omega_{j'})}{N_F} \hat{\tau}_3 \hat{G}_{m\mathbf{k}+\mathbf{q}}(i\omega_{j'}) \hat{\tau}_3. \quad (22)$$

The non-adiabatic self-energy $\hat{\Sigma}_{n\mathbf{k}}^{(\text{NA})}(i\omega_j)$, corresponding to the second-order Feynman diagram in Fig. 1(b), is given by

$$\hat{\Sigma}_{n\mathbf{k}}^{(\text{NA})}(i\omega_j) = (k_B T)^2 \sum_{mlp} \sum_{\mathbf{q}\mathbf{p}} \sum_{\nu\mu} \sum_{j'j''} g_{m\mathbf{k}+\mathbf{q},n\mathbf{k}}^{\mathbf{q}\nu} g_{l\mathbf{k}+\mathbf{q}+\mathbf{p},m\mathbf{k}+\mathbf{q}}^{\mathbf{p}\mu} g_{p\mathbf{k}+\mathbf{p},l\mathbf{k}+\mathbf{q}+\mathbf{p}}^{-\mathbf{q}\mu} g_{n\mathbf{k},p\mathbf{k}+\mathbf{p}}^{-\mathbf{p}\mu} D_{\mathbf{q}\nu}(i\omega_j - i\omega_{j'}) D_{\mathbf{p}\mu}(i\omega_j - i\omega_{j''}) \times \hat{\tau}_3 \hat{G}_{m\mathbf{k}+\mathbf{q}}(i\omega_{j'}) \hat{\tau}_3 \hat{G}_{l\mathbf{k}+\mathbf{q}+\mathbf{p}}(i\omega_{j''} - i\omega_j + i\omega_{j'}) \hat{\tau}_3 \hat{G}_{p\mathbf{k}+\mathbf{p}}(i\omega_{j''}) \hat{\tau}_3. \quad (23)$$

Here, each matrix element represents an e-ph scattering vertex, associated with either phonon absorption ($\mathbf{q}\nu$ or $\mathbf{p}\mu$) or phonon emission ($-\mathbf{q}\nu$ or $-\mathbf{p}\mu$). The expression captures a two-phonon scattering process involving four distinct interactions, each requiring explicit evaluation of the corresponding matrix element.

Analogous to the adiabatic case, we substitute the phonon propagators with their bare counterparts and introduce the anisotropic first-order vertex correction to the e-ph coupling via a double spectral representation

$$\lambda_{n\mathbf{k},m\mathbf{k}+\mathbf{q},l\mathbf{k}+\mathbf{q}+\mathbf{p},p\mathbf{k}+\mathbf{p}}^V(i\omega_j - i\omega_{j'}, i\omega_j - i\omega_{j''}) = \int_0^\infty d\omega \int_0^\infty d\omega' \frac{2\omega}{(\omega_j - \omega_{j'})^2 + \omega^2} \times \frac{2\omega'}{(\omega_j - \omega_{j''})^2 + \omega'^2} \times \alpha^2 F_{n\mathbf{k},m\mathbf{k}+\mathbf{q},l\mathbf{k}+\mathbf{q}+\mathbf{p},p\mathbf{k}+\mathbf{p}}^V(\omega, \omega'), \quad (24)$$

where the anisotropic first-order vertex correction to the Eliashberg spectral function is expressed as follows

$$\alpha^2 F_{n\mathbf{k},m\mathbf{k}+\mathbf{q},l\mathbf{k}+\mathbf{q}+\mathbf{p},p\mathbf{k}+\mathbf{p}}^V(\omega, \omega') = N_F^2 \sum_{\nu\mu} g_{m\mathbf{k}+\mathbf{q},n\mathbf{k}}^{\mathbf{q}\nu} g_{l\mathbf{k}+\mathbf{q}+\mathbf{p},m\mathbf{k}+\mathbf{q}}^{\mathbf{p}\mu} g_{p\mathbf{k}+\mathbf{p},l\mathbf{k}+\mathbf{q}+\mathbf{p}}^{-\mathbf{q}\mu} g_{n\mathbf{k},p\mathbf{k}+\mathbf{p}}^{-\mathbf{p}\mu} \delta(\omega - \omega_{\mathbf{q}\nu}) \delta(\omega' - \omega_{\mathbf{p}\mu}). \quad (25)$$

Using Eqs. (24) and (25), the non-adiabatic electron self-energy can be expressed in a compact form as

$$\hat{\Sigma}_{n\mathbf{k}}^{(\text{NA})}(i\omega_j) = \frac{(k_B T)^2}{N_F^2} \sum_{mlp} \sum_{\mathbf{q}\mathbf{p}} \sum_{j'j''} \hat{\tau}_3 \hat{G}_{m\mathbf{k}+\mathbf{q}}(i\omega_{j'}) \hat{\tau}_3 \hat{G}_{l\mathbf{k}+\mathbf{q}+\mathbf{p}}(i\omega_{j''} - i\omega_j + i\omega_{j'}) \hat{\tau}_3 \hat{G}_{p\mathbf{k}+\mathbf{p}}(i\omega_{j''}) \hat{\tau}_3 \times \lambda_{n\mathbf{k},m\mathbf{k}+\mathbf{q},l\mathbf{k}+\mathbf{q}+\mathbf{p},p\mathbf{k}+\mathbf{p}}^V(i\omega_j - i\omega_{j'}, i\omega_j - i\omega_{j''}). \quad (26)$$

B. Isotropic approximation to electron self-energy

Accounting for the anisotropy in the non-adiabatic self-energy is computationally demanding, as Eq. (23) involves Brillouin zone integrals over two crystal momenta. To date, the most advanced calculations of su-

perconducting properties with anisotropic vertex corrections have relied on several approximations, which include using model Hamiltonians for electronic states, an isotropic Einstein phonon spectrum, and a single e-ph coupling parameter [48]. However, for most materials, except for a few notable layered systems such as MgB₂-

type superconductors [56, 82, 83], graphite intercalation compounds [84, 85], and transition metal dichalcogenides [86, 87], the effect of this full momentum dependence is weak and an isotropic treatment can be employed [19, 21]. This approximation consists of replacing the \mathbf{k} -dependent quantities with their Fermi-surface averages. A detailed derivation is provided in Sec. II of the Supplementary Information [62].

Within the isotropic approximation, the adiabatic self-energy takes the following form

$$\hat{\Sigma}^{(A)}(i\omega_j) = \frac{k_B T}{N_F} \sum_{j'} \lambda(i\omega_j - i\omega_{j'}) \int_{-\infty}^{\infty} d\varepsilon' N(\varepsilon') \hat{\tau}_3 \hat{G}(\varepsilon', i\omega_{j'}) \hat{\tau}_3, \quad (27)$$

where $\lambda(i\omega_j - i\omega_{j'})$ is the isotropic e-ph kernel, expressed

as

$$\lambda(i\omega_j - i\omega_{j'}) = \int_0^{\infty} d\omega \frac{2\omega}{(\omega_j - \omega_{j'})^2 + \omega^2} \alpha^2 F(\omega). \quad (28)$$

The kernel is an even function of the Matsubara frequency and attains its maximum at $\omega_j - \omega_{j'} = 0$

$$\lambda = 2 \int_0^{\infty} d\omega \frac{\alpha^2 F(\omega)}{\omega}, \quad (29)$$

where λ denotes the isotropic e-ph coupling strength. The isotropic Eliashberg spectral function $\alpha^2 F(\omega)$ represents the double Fermi-surface average of $\alpha^2 F_{n\mathbf{k}, m\mathbf{k}+\mathbf{q}}(\omega)$ and is given by

$$\alpha^2 F(\omega) = \frac{1}{N_F} \sum_{nm} \sum_{\mathbf{kq}} \delta(\varepsilon_{n\mathbf{k}} - \varepsilon_F) \delta(\varepsilon_{m\mathbf{k}+\mathbf{q}} - \varepsilon_F) \times \sum_{\nu} |g_{m\mathbf{k}+\mathbf{q}, n\mathbf{k}}^{\mathbf{q}\nu}|^2 \delta(\omega - \omega_{\mathbf{q}\nu}), \quad (30)$$

Following similar steps, the isotropic non-adiabatic self-energy associated with the lowest-order vertex correction can be simplified as

$$\begin{aligned} \hat{\Sigma}^{(NA)}(i\omega_j) = & \frac{(k_B T)^2}{N_F^2} \sum_{j'j''} \lambda^V(i\omega_j - i\omega_{j'}, i\omega_j - i\omega_{j''}) \int_{-\infty}^{\infty} d\varepsilon' N(\varepsilon') \int_{-\infty}^{\infty} d(\varepsilon'' - \varepsilon + \varepsilon') N(\varepsilon'' - \varepsilon + \varepsilon') \int_{-\infty}^{\infty} d\varepsilon'' N(\varepsilon'') \\ & \times \hat{\tau}_3 \hat{G}(\varepsilon', i\omega_{j'}) \hat{\tau}_3 \hat{G}(\varepsilon'' - \varepsilon + \varepsilon', i\omega_{j''} - i\omega_j + i\omega_{j'}) \hat{\tau}_3 \hat{G}(\varepsilon'', i\omega_{j''}) \hat{\tau}_3, \end{aligned} \quad (31)$$

where the isotropic vertex-corrected e-ph kernel

$$\lambda^V(i\omega_j - i\omega_{j'}, i\omega_j - i\omega_{j''}) = \int_0^{\infty} d\omega \frac{2\omega}{(\omega_j - \omega_{j'})^2 + \omega^2} \int_0^{\infty} d\omega' \frac{2\omega'}{(\omega_j - \omega_{j''})^2 + \omega'^2} \alpha^2 F^V(\omega, \omega'). \quad (32)$$

The vertex-corrected kernel attains its maximum at $i\omega_j - i\omega_{j'} = 0$ and $i\omega_j - i\omega_{j''} = 0$, and reduces to

$$\lambda^V = 4 \int_0^{\infty} d\omega \int_0^{\infty} d\omega' \frac{\alpha^2 F^V(\omega, \omega')}{\omega \omega'}. \quad (33)$$

Here, λ^V is called the vertex-corrected e-ph coupling strength and is a dimensionless measure of the average e-ph coupling strength arising from the non-adiabatic vertex corrections. The isotropic vertex-corrected Eliashberg spectral function $\alpha^2 F^V(\omega, \omega')$ is obtained by performing the Fermi-surface average as follows

$$\alpha^2 F^V(\omega, \omega') = \frac{1}{C(0)} \sum_{nmlp} \sum_{\mathbf{kqp}} \delta(\varepsilon_{n\mathbf{k}} - \varepsilon_F) \delta(\varepsilon_{m\mathbf{k}+\mathbf{q}} - \varepsilon_F) \delta(\varepsilon_{l\mathbf{k}+\mathbf{q}+\mathbf{p}} - \varepsilon_F) \delta(\varepsilon_{p\mathbf{k}+\mathbf{p}} - \varepsilon_F) \alpha^2 F_{n\mathbf{k}, m\mathbf{k}+\mathbf{p}, l\mathbf{k}+\mathbf{q}+\mathbf{p}, p\mathbf{k}+\mathbf{p}}^V(\omega, \omega'). \quad (34)$$

Here, the normalization factor $C(0)$ corresponds to the total weight of all four-fold combinations of states at ε_F

$$\begin{aligned} C(0) = & \sum_{nmlp} \sum_{\mathbf{kqp}} \delta(\varepsilon_{n\mathbf{k}} - \varepsilon_F) \delta(\varepsilon_{m\mathbf{k}+\mathbf{q}} - \varepsilon_F) \\ & \times \delta(\varepsilon_{l\mathbf{k}+\mathbf{q}+\mathbf{p}} - \varepsilon_F) \delta(\varepsilon_{p\mathbf{k}+\mathbf{p}} - \varepsilon_F). \end{aligned} \quad (35)$$

Computing Eq. (34) has remained a longstanding challenge, even in the isotropic framework, due to the requirement of evaluating four e-ph matrix elements in-

volving two different phonons. To date, additional approximations have been employed, such as estimating the density factor $C(0)$ based on the free-electron model [25, 55], and expressing the vertex-corrected e-ph term $\lambda^V(i\omega_j - i\omega_{j'}, i\omega_j - i\omega_{j''})$ as a product of two e-ph vertices $\lambda(i\omega_j - i\omega_{j'}) \lambda(i\omega_j - i\omega_{j''})$ [48, 55]. In this work, we compute this term without relying on these simplifications. We exploit the symmetry under phonon exchange $(\mathbf{q}, \nu, \omega) \leftrightarrow (\mathbf{p}, \mu, \omega')$ to reduce the computational

cost. This symmetry, evident from the Feynman diagrams in Fig. 1(b), enables us to express $\alpha^2 F^V(\omega, \omega')$ in terms of the real part of the four e-ph matrix elements product. A detailed derivation is provided in Sec. III of the Supplementary Information [62].

C. Isotropic non-adiabatic full-bandwidth Eliashberg equations

To obtain the Eliashberg equations, the standard procedure is to express the total self-energy on the basis of

Pauli matrices in terms of three scalar functions [4, 5, 8]:

$$\hat{\Sigma}(i\omega_j) = i\omega_j [1 - Z(i\omega_j)] \hat{\tau}_0 + \chi(i\omega_j) \hat{\tau}_3 + \phi(i\omega_j) \hat{\tau}_1, \quad (36)$$

where $Z(i\omega_j)$ is the mass renormalization function, $\chi(i\omega_j)$ is the energy shift, and $\phi(i\omega_j)$ is the order parameter. The quantity $\Delta(i\omega_j) = \phi(i\omega_j)/Z(i\omega_j)$ defines the superconducting gap function. Through the Dyson equation (10), the calculation of the Green's function $\hat{G}(\varepsilon, i\omega_{j'})$ is reduced to solving three coupled equations for $Z(i\omega_j)$, $\chi(i\omega_j)$, and $\phi(i\omega_j)$. A detailed derivation is given in Sec. IV of Supplemental Information [62]. We refer to this final set as the isotropic non-adiabatic full-bandwidth (NA-FBW) Eliashberg equations and are given by

$$\begin{aligned} Z(i\omega_j) = 1 + & \frac{k_B T}{N_F \omega_j} \sum_{j'} \lambda(i\omega_j - i\omega_{j'}) \int_{-\infty}^{\infty} d\varepsilon' N(\varepsilon') \gamma^Z(\varepsilon', i\omega_{j'}) \\ & + \frac{(k_B T)^2}{N_F^2 \omega_j} \sum_{j' j''} \lambda^V(i\omega_j - i\omega_{j'}, i\omega_j - i\omega_{j''}) \int_{-\infty}^{\infty} d\varepsilon' N(\varepsilon') \int_{-\infty}^{\infty} d(\varepsilon'' + \varepsilon' - \varepsilon) N(\varepsilon'' + \varepsilon' - \varepsilon) \int_{-\infty}^{\infty} d\varepsilon'' N(\varepsilon'') \\ & \times \left[\gamma^T(\varepsilon', i\omega_{j'}) P^Z(\varepsilon'' + \varepsilon' - \varepsilon, i\omega_{j''} - i\omega_j + i\omega_{j'}) \gamma(\varepsilon'', i\omega_{j''}) \right], \end{aligned} \quad (37)$$

$$\begin{aligned} \chi(i\omega_j) = & -\frac{k_B T}{N_F} \sum_{j'} \lambda(i\omega_j - i\omega_{j'}) \int_{-\infty}^{\infty} d\varepsilon' N(\varepsilon') \gamma^X(\varepsilon', i\omega_{j'}) \\ & - \frac{(k_B T)^2}{N_F^2} \sum_{j' j''} \lambda^V(i\omega_j - i\omega_{j'}, i\omega_j - i\omega_{j''}) \int_{-\infty}^{\infty} d\varepsilon' N(\varepsilon') \int_{-\infty}^{\infty} d(\varepsilon'' + \varepsilon' - \varepsilon) N(\varepsilon'' + \varepsilon' - \varepsilon) \int_{-\infty}^{\infty} d\varepsilon'' N(\varepsilon'') \\ & \times \left[\gamma^T(\varepsilon', i\omega_{j'}) P^X(\varepsilon'' + \varepsilon' - \varepsilon, i\omega_{j''} - i\omega_j + i\omega_{j'}) \gamma(\varepsilon'', i\omega_{j''}) \right], \end{aligned} \quad (38)$$

$$\begin{aligned} \phi(i\omega_j) = & \frac{k_B T}{N_F} \sum_{j'} [\lambda(i\omega_j - i\omega_{j'}) - \mu_E^*] \int_{-\infty}^{\infty} d\varepsilon' N(\varepsilon') \gamma^\phi(\varepsilon', i\omega_{j'}) \\ & + \frac{(k_B T)^2}{N_F^2} \sum_{j' j''} \lambda^V(i\omega_j - i\omega_{j'}, i\omega_j - i\omega_{j''}) \int_{-\infty}^{\infty} d\varepsilon' N(\varepsilon') \int_{-\infty}^{\infty} d(\varepsilon'' + \varepsilon' - \varepsilon) N(\varepsilon'' + \varepsilon' - \varepsilon) \int_{-\infty}^{\infty} d\varepsilon'' N(\varepsilon'') \\ & \times \left[\gamma^T(\varepsilon', i\omega_{j'}) P^\phi(\varepsilon'' + \varepsilon' - \varepsilon, i\omega_{j''} - i\omega_j + i\omega_{j'}) \gamma(\varepsilon'', i\omega_{j''}) \right], \end{aligned} \quad (39)$$

$$N_e = \int_{-\infty}^{\infty} d\varepsilon' N(\varepsilon') \left[1 - 2k_B T \sum_{j'} \frac{\varepsilon - \mu_F + \chi(i\omega_{j'})}{\Theta(\varepsilon, i\omega_{j'})} \right]. \quad (40)$$

In Eq. (40), N_e represents the electron number that determines the chemical potential which is updated self-consistently [9, 57, 58]. This is referred to as FBW+ μ , while calculations performed with a fixed $\mu_F = \varepsilon_F$ are denoted simply as FBW [57, 58]. The Coulomb interaction enters the Eliashberg expression only through Eq. (39), where it is approximated by the semi-empirical pseudopotential μ_E^* introduced earlier. The summation over the Matsubara frequencies in Eqs. (37)–(40) formally ex-

tends from $-\infty$ to $+\infty$, however, in practical calculations, it is evaluated over positive Matsubara frequencies only and truncated at a cutoff frequency, as detailed in Sec. V of the Supplementary Information [62].

Above, we follow Ref. [48] and introduce the pseudo-

vector $\gamma(\varepsilon, i\omega_j)$ as

$$\gamma(\varepsilon, i\omega_j) = \begin{pmatrix} \gamma^Z(\varepsilon, i\omega_j) \\ \gamma^X(\varepsilon, i\omega_j) \\ \gamma^\phi(\varepsilon, i\omega_j) \end{pmatrix}, \quad (41)$$

and its transpose is given by

$$\gamma^T(\varepsilon, i\omega_j) = (\gamma^Z(\varepsilon, i\omega_j) \quad \gamma^X(\varepsilon, i\omega_j) \quad \gamma^\phi(\varepsilon, i\omega_j)), \quad (42)$$

along with the matrices $P^Z(\varepsilon, i\omega_j)$, $P^X(\varepsilon, i\omega_j)$, and $P^\phi(\varepsilon, i\omega_j)$ defined as follows

$$P^Z(\varepsilon, i\omega_j) = \begin{pmatrix} -\gamma^Z(\varepsilon, i\omega_j) & \gamma^X(\varepsilon, i\omega_j) & -\gamma^\phi(\varepsilon, i\omega_j) \\ \gamma^X(\varepsilon, i\omega_j) & \gamma^Z(\varepsilon, i\omega_j) & 0 \\ -\gamma^\phi(\varepsilon, i\omega_j) & 0 & \gamma^Z(\varepsilon, i\omega_j) \end{pmatrix}, \quad (43)$$

$$P^X(\varepsilon, i\omega_j) = \begin{pmatrix} -\gamma^X(\varepsilon, i\omega_j) & -\gamma^Z(\varepsilon, i\omega_j) & 0 \\ -\gamma^Z(\varepsilon, i\omega_j) & \gamma^X(\varepsilon, i\omega_j) & -\gamma^\phi(\varepsilon, i\omega_j) \\ 0 & -\gamma^\phi(\varepsilon, i\omega_j) & -\gamma^X(\varepsilon, i\omega_j) \end{pmatrix}, \quad (44)$$

$$P^\phi(\varepsilon, i\omega_j) = \begin{pmatrix} \gamma^\phi(\varepsilon, i\omega_j) & 0 & -\gamma^Z(\varepsilon, i\omega_j) \\ 0 & \gamma^\phi(\varepsilon, i\omega_j) & \gamma^X(\varepsilon, i\omega_j) \\ -\gamma^Z(\varepsilon, i\omega_j) & \gamma^X(\varepsilon, i\omega_j) & -\gamma^\phi(\varepsilon, i\omega_j) \end{pmatrix}. \quad (45)$$

The elements of $\gamma(\varepsilon, i\omega_j)$, $P^Z(\varepsilon, i\omega_j)$, $P^X(\varepsilon, i\omega_j)$, and $P^\phi(\varepsilon, i\omega_j)$ are given by

$$\gamma^Z(\varepsilon, i\omega_j) = \frac{\omega_j Z(i\omega_j)}{\Theta(\varepsilon, i\omega_j)}, \quad (46)$$

$$\gamma^X(\varepsilon, i\omega_j) = \frac{\varepsilon - \mu_F + \chi(i\omega_j)}{\Theta(\varepsilon, i\omega_j)}, \quad (47)$$

$$\gamma^\phi(\varepsilon, i\omega_j) = \frac{\phi(i\omega_j)}{\Theta(\varepsilon, i\omega_j)}, \quad (48)$$

with

$$\Theta(\varepsilon, i\omega_j) = [\omega_j Z(i\omega_j)]^2 + [\varepsilon - \mu_F + \chi(i\omega_j)]^2 + [\phi(i\omega_j)]^2. \quad (49)$$

D. Isotropic non-adiabatic Fermi-surface restricted Eliashberg equations

We can further simplify the isotropic NA-FBW Eliashberg equations by adopting the constant DOS approximation, such that $N(\varepsilon) \rightarrow N_F$. Assuming an infinite electronic bandwidth at half-filling, the energy integral can be evaluated analytically, as detailed in Sec. VI of the Supplementary Information [62], leading to the isotropic non-adiabatic Fermi-surface restricted (NA-FSR) Eliashberg equations

$$\begin{aligned} Z(i\omega_j) = & 1 + \frac{\pi k_B T}{\omega_j} \sum_{j'} \lambda(i\omega_j - i\omega_{j'}) \tilde{\gamma}^Z(i\omega_{j'}) \\ & + \frac{\pi^3 (k_B T)^2 N_F}{\omega_j} \sum_{j'} \sum_{j''} \lambda^V(i\omega_j - i\omega_{j'}, i\omega_j - i\omega_{j''}) \\ & \times \left[\tilde{\gamma}^T(i\omega_{j'}) \tilde{P}^\omega(i\omega_{j''} - i\omega_j + i\omega_{j'}) \tilde{\gamma}(i\omega_{j''}) \right], \quad (50) \end{aligned}$$

$$\begin{aligned} \Delta(i\omega_j) Z(i\omega_j) = & \pi k_B T \sum_{j'} [\lambda(i\omega_j - i\omega_{j'}) - \mu_E^*] \tilde{\gamma}^\phi(i\omega_{j'}) \\ & + \pi^3 (k_B T)^2 N_F \sum_{j'} \sum_{j''} \lambda^V(i\omega_j - i\omega_{j'}, i\omega_j - i\omega_{j''}) \\ & \times \left[\tilde{\gamma}^T(i\omega_{j'}) \tilde{P}^\Delta(i\omega_{j''} - i\omega_j + i\omega_{j'}) \tilde{\gamma}(i\omega_{j''}) \right]. \quad (51) \end{aligned}$$

The pseudo-vector $\tilde{\gamma}(\varepsilon, i\omega_j)$ and its transpose $\tilde{\gamma}^T(\varepsilon, i\omega_j)$, along with the matrices $\tilde{P}^\omega(i\omega_j)$ and $\tilde{P}^\Delta(i\omega_j)$ are expressed as

$$\tilde{\gamma}(i\omega_j) = \begin{pmatrix} \tilde{\gamma}^\omega(i\omega_j) \\ \tilde{\gamma}^\Delta(i\omega_j) \end{pmatrix}, \quad \tilde{\gamma}^T(i\omega_j) = (\gamma^\omega(i\omega_j) \quad \gamma^\Delta(i\omega_j)), \quad (52)$$

$$\tilde{P}^\omega(i\omega_j) = \begin{pmatrix} -\tilde{\gamma}^\omega(i\omega_j) & -\tilde{\gamma}^\Delta(i\omega_j) \\ -\tilde{\gamma}^\Delta(i\omega_j) & \tilde{\gamma}^\omega(i\omega_j) \end{pmatrix}, \quad (53)$$

$$\tilde{P}^\Delta(i\omega_j) = \begin{pmatrix} \tilde{\gamma}^\Delta(i\omega_j) & -\tilde{\gamma}^\omega(i\omega_j) \\ -\tilde{\gamma}^\omega(i\omega_j) & -\tilde{\gamma}^\Delta(i\omega_j) \end{pmatrix}, \quad (54)$$

where we define

$$\tilde{\gamma}^\omega(i\omega_j) = \frac{\omega_j}{\sqrt{\omega_j^2 + \Delta^2(i\omega_j)}}, \quad (55a)$$

$$\tilde{\gamma}^\Delta(i\omega_j) = \frac{\Delta(i\omega_j)}{\sqrt{\omega_j^2 + \Delta^2(i\omega_j)}}, \quad (55b)$$

with $\Delta(i\omega_j) = \phi(i\omega_j)/Z(i\omega_j)$ being the superconducting gap function.

III. COMPUTATIONAL METHODS

We employed the Quantum ESPRESSO (QE) package [88] with optimized norm-conserving Vanderbilt pseudopotentials (ONCVPSP) [89] from the Hamman's library generated with the Perdew-Burke-Ernzerhof parametrization [90]. We used plane-wave cutoffs of 60 and 100 Ry, a Methfessel-Paxton smearing [91] value of 0.01 Ry, and Γ -centered \mathbf{k} -grids of $24 \times 24 \times 24$ and $16 \times 16 \times 16$ to describe the electronic structure of H_3S and Pb, respectively. The lattice parameters and atomic positions were relaxed until the total energy was converged within 10^{-6} Ry and the maximum force on each atom was less than 10^{-4} Ry/Å. The dynamical matrices and the linear variation of the self-consistent potential were calculated within DFPT [69] on \mathbf{q} -meshes of $4 \times 4 \times 4$ and $8 \times 8 \times 8$ for H_3S and Pb, respectively.

For H_3S at 200 GPa, we carried out a series of convergence tests to ensure the reliability of our phonon calculations. First, we computed the phonon dispersion by varying the \mathbf{q} -mesh from $2 \times 2 \times 2$ to $8 \times 8 \times 8$ (see Fig. S3(a) [62]). Notably, imaginary modes appear when using a $3 \times 3 \times 3$ \mathbf{q} -grid, which are eliminated upon including anharmonic corrections. To reduce the computational cost, we examined the convergence of the phonon dispersion with

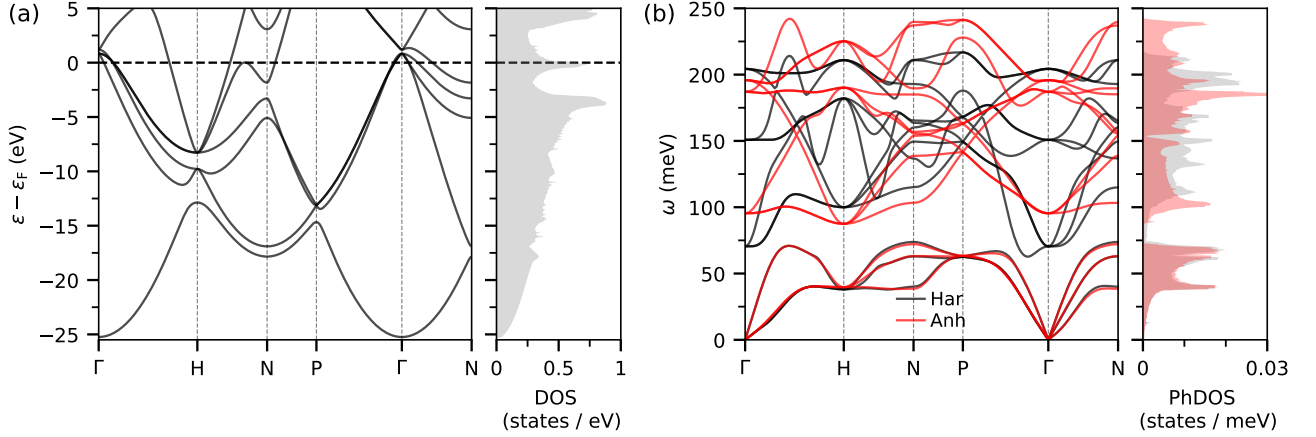


FIG. 2. (a) Electronic band structure and total density of states (DOS), highlighting the vHs peak near ε_F , and (b) phonon dispersion and phonon density of states (PhDOS) computed within the harmonic (black solid lines) and anharmonic approximations (red solid lines) for H_3S at 200 GPa.

respect to the kinetic energy cutoff by lowering it from 100 Ry to 60 Ry. The results in Fig. S3(b) [62] show that a 60 Ry cutoff yields converged phonon frequencies and is therefore used throughout this work.

We computed the anharmonic phonons for H_3S with the anharmonic special displacement method (ASDM) [64, 92] implemented in the ZG code of EPW [57]. Calculations were performed for $2 \times 2 \times 2$, $3 \times 3 \times 3$, and $4 \times 4 \times 4$ supercells corresponding to 192, 648, and 1,536 distorted configurations, respectively. An $12 \times 12 \times 12$ \mathbf{k} -grid for the primitive unit cell was found to be enough to extract the interatomic force constants (IFCs) for the anharmonic phonon dispersions, drastically reducing the computational cost (see Fig. S4(a) [62]). All anharmonic calculations presented here were performed at 0 K.

The EPW code [13, 56, 57, 67] was used to investigate e-ph interactions and superconducting properties. The electronic wavefunctions required for the Wannier interpolation [93–95] were obtained on a uniform Γ -centered $8 \times 8 \times 8$ \mathbf{k} -grid. For H_3S , we used ten atom-centered orbitals to describe the electronic structure, with one s orbital for each H atom and five $s, p, d_{xy}, d_{xz}, d_{yz}$ orbitals for the S atom, while for Pb we used four sp^3 orbitals. The isotropic Eliashberg spectral functions were computed using uniform $48 \times 48 \times 48$ \mathbf{k} - and $24 \times 24 \times 24$ \mathbf{q} -point grids for electrons and phonons, respectively. The isotropic Eliashberg equations were solved on the imaginary Matsubara frequency axis, using an energy cutoff of 2.5 eV for H_3S and 1 eV for Pb. Dirac delta functions for electrons and phonons were approximated by Gaussians with widths of 50 meV and 2.5 meV for H_3S , and 50 meV and 1.5 meV for Pb. In the case of H_3S , the DOS, e-ph coupling, and superconducting gap are highly sensitive to the position of the Fermi level due to the vHs located near ε_F . To ensure consistency and numerical accuracy, ε_F was set to the value obtained from EPW calculations using a $48 \times 48 \times 48$ \mathbf{k} -grid for both H_3S and Pb. In

addition, we found that to achieve convergence of the superconducting gap and critical temperature in the FBW calculations, an energy window of at least 1 eV for H_3S and Pb is required when computing the DOS.

IV. RESULTS AND DISCUSSION

A. Electronic structure and phonon dispersion of H_3S

At 200 GPa, H_3S crystallizes in the high-symmetry $Im\bar{3}m$ phase with a lattice parameter of 3.089 Å, consistent with previous theoretical studies [60, 96, 97]. The band structure, shown in Fig. 2(a), exhibits a broad bandwidth of approximately 25 eV below ε_F , with parabolic dispersion for the deeper lying bands. The corresponding DOS features two prominent valleys at approximately -1.75 eV and 2.50 eV, as well as a sharp vHs peak near ε_F . This vHs significantly enhances the e-ph coupling strength, which is a key factor in the high T_c of H_3S [24, 98–100]. At higher pressures, the vHs peak shifts away from ε_F , leading to a decrease in the DOS at ε_F and a corresponding suppression of T_c [101]. Additionally, the width of the vHs effectively defines a low Fermi energy scale (~ 300 meV), reducing the Fermi velocity v_F and raising questions about the validity of Migdal’s approximation in this system [23, 27].

Figure 2(b) compares the phonon dispersion and phonon density of states (PhDOS), calculated within the harmonic and anharmonic approximations. The phonon spectrum exhibits a clear separation between low-frequency acoustic modes (below 75 meV), mainly arising from sulfur vibrations, and high-frequency optical modes (above 75 meV), primarily involving hydrogen. This separation is a direct consequence of the large mass difference between S and H atoms.

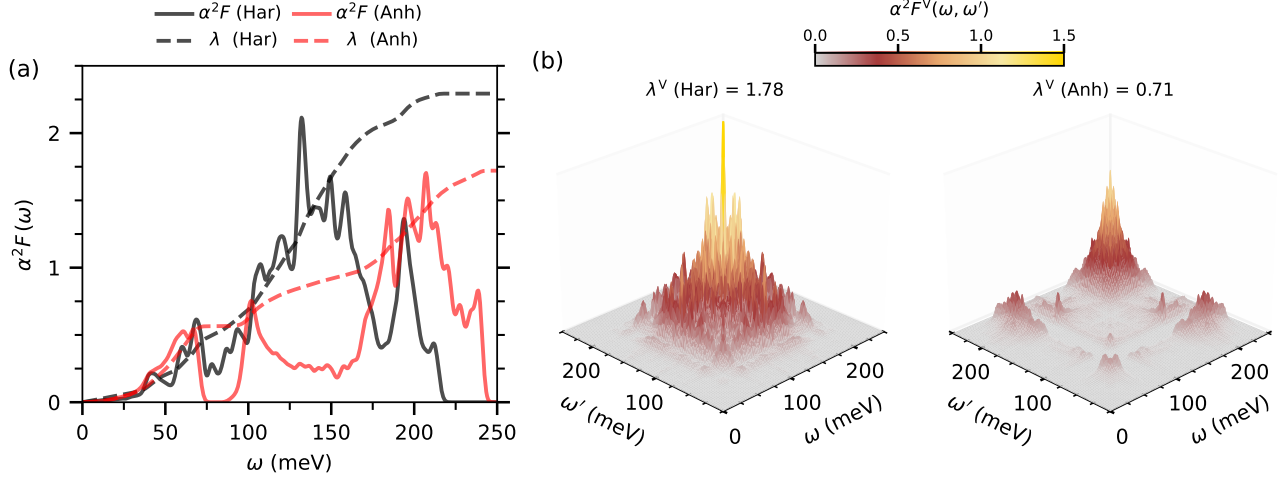


FIG. 3. (a) Eliashberg spectral function $\alpha^2 F(\omega)$ and integrated e-ph coupling strength $\lambda(\omega)$ for both harmonic and anharmonic phonons within the adiabatic Migdal approximation, and (b) vertex-corrected Eliashberg spectral function $\alpha^2 F^V(\omega, \omega')$ and integrated vertex-corrected e-ph coupling strength λ^V with harmonic (left) and anharmonic (right) phonons for H₃S at 200 GPa.

For the anharmonic calculations, convergence was verified with respect to both the atomic displacement amplitude and the supercell size, as detailed in Sec. VII of the Supporting Information (see Fig. S4(b) and S5) [62]. The low-frequency phonon modes are largely unaffected by anharmonicity, in line with a previous study [60]. This insensitivity stems from the heavier mass and smaller vibrational amplitudes of sulfur atoms, which make them less responsive to anharmonic effects. In contrast, the high-frequency optical modes undergo substantial anharmonic renormalization, with hardening of up to 30 meV observed along several high-symmetry directions. The PhDOS further reinforces this picture. While the spectral features associated with sulfur vibrations remain nearly intact, the high-frequency region shows significant broadening extending up to 243 meV. Accurately capturing these anharmonic effects is essential for a reliable description of vibrational dynamics and superconducting properties of H₃S.

B. Vertex-corrected electron-phonon coupling in H₃S

The Eliashberg spectral function and the corresponding cumulative e-ph coupling strength for H₃S at 200 GPa are shown in Fig. 3(a). The harmonic $\alpha^2 F(\omega)$ features a broad central peak spanning the 75–175 meV range, accompanied by a smaller peak at lower frequencies and a distinct sharp peak at 194 meV. As a result, the cumulative $\lambda(\omega)$ increases steadily, with the acoustic region contributing approximately 0.48, and continues to rise throughout the spectrum, ultimately reaching a total value of $\lambda = 2.29$, consistent with previous reports [18, 20, 58, 96].

When anharmonic effects are included, both phonon frequencies and eigenvectors are renormalized, which in turn modifies the e-ph matrix elements according to Eq. (8). The cumulative e-ph coupling strength $\lambda(\omega)$ from the sulfur-dominated regions increases slightly to 0.56, consistent with the observation that acoustic phonon frequencies are only weakly affected by anharmonicity. Above 75 meV, $\alpha^2 F(\omega)$ exhibits two well-separated peaks, corresponding to the softening of the bond-bending and hardening of bond-stretching H modes, respectively. Among these, the bond-stretching modes contribute most significantly to λ . In line with a prior study [60], our anharmonic analysis shows a 25% reduction in the e-ph coupling strength, resulting in a revised total value of 1.72.

As discussed earlier, the coexistence of high-frequency hydrogen phonon modes and a low Fermi energy raises concerns about the validity of the standard Migdal approximation in H₃S [23–25, 27] and requires taking higher-order vertex corrections into account beyond conventional ME theory. To our knowledge, this work presents the first quantitative computation of the full isotropic lowest-order vertex-corrected Eliashberg spectral function $\alpha^2 F^V(\omega, \omega')$ for this system.

Figure 3(b) shows 3D plots of $\alpha^2 F^V(\omega, \omega')$, comparing results based on harmonic (left panel) and anharmonic (right panel) phonons. In the harmonic case, $\alpha^2 F^V(\omega, \omega')$ displays a broad distribution across the mid- to high-frequency phonon spectrum, with dominant contributions concentrated between 75 and 200 meV. In contrast, the low-frequency acoustic region contributes negligibly, indicating that sulfur modes have minimal impact once vertex corrections are included. The integrated vertex-corrected coupling strength is $\lambda^V = 1.78$, approximately 78% of the corresponding adiabatic value $\lambda = 2.29$.

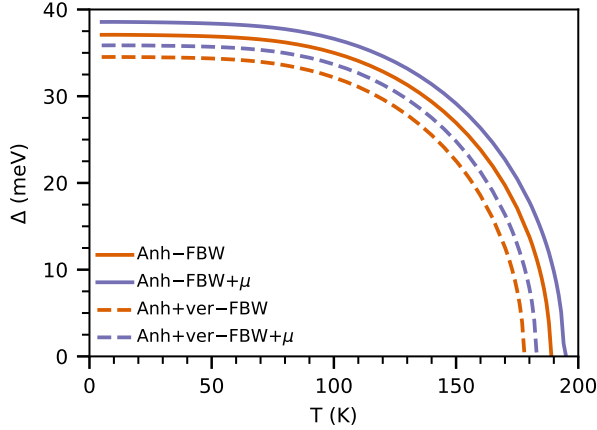


FIG. 4. Isotropic superconducting gap $\Delta(T)$ for H_3S , calculated with anharmonic phonons using four different approaches: adiabatic FBW (solid orange), adiabatic FBW+ μ (solid purple), vertex-corrected FBW (dashed orange), and vertex-corrected FBW+ μ (dashed purple) with a Coulomb parameter $\mu_E^* = 0.16$.

In the anharmonic case, $\alpha^2 F^V(\omega, \omega')$ is fragmented, with spectral weight confined in narrower regions of the (ω, ω') plane. Unlike the harmonic scenario, small intensity peaks emerge in the low-frequency acoustic region, reflecting changes in phonon eigenvectors induced by anharmonicity. At mid-frequencies, the spectral weight is reduced and shifts toward higher energies due to the hardening of hydrogen modes. The total vertex-corrected e-ph coupling strength is substantially reduced, with $\lambda^V = 0.71$, representing nearly a 60% decrease compared to the harmonic vertex-corrected value.

C. Superconducting gap of H_3S with vertex corrections

The superconducting properties of H_3S have been extensively investigated, with previous calculations primarily based on the adiabatic ME formalism without vertex corrections, using either the FSR [60, 96] or FBW approach [21, 24, 58]. Although the potential significance of vertex corrections has been acknowledged [26], earlier isotropic treatments relied on simplified models, either a single Einstein phonon spectrum [17, 24] or empirical modifications to the vertex-corrected e-ph kernel $\lambda^V(i\omega_j - i\omega_{j'}, i\omega_j - i\omega_{j''})$ [25].

In this work, we go beyond such approximations and solve the isotropic Eliashberg equations using the full vertex-corrected e-ph spectral function $\alpha^2 F^V(\omega, \omega')$, computed from first principles. Several studies on H_3S [17, 24, 58] have emphasized the importance of the FBW description, owing to its narrow electronic bands and the presence of critical features near ε_F , such as vHs and Lifshitz transitions [23, 26]. To capture these effects, we compute the isotropic superconducting gap $\Delta(T)$ using

both the FBW and FBW+ μ approaches, with and without vertex corrections, while also incorporating anharmonic phonons, as shown in Fig. 4. These calculations explicitly include the energy dependence of the electronic DOS. Consistent with previous studies on H_3S [58, 60], we adopt a Coulomb pseudopotential value of $\mu_E^* = 0.16$. When solving the Eliashberg expressions, this choice, combined with an electronic bandwidth ε_{el} in the range of 10–25 eV corresponds to $\mu_c = 0.21$ –0.25 via Eqs. (15) and (16), in agreement with values computed *ab initio* [18, 75, 77].

As shown in Fig. 4, the adiabatic FBW approach yields a zero-temperature superconducting gap of $\Delta(0) = 37.1$ meV, closing at a critical temperature $T_c \approx 189$ K. When the chemical potential is updated self-consistently within the FBW+ μ scheme, both the gap and T_c increase slightly to 38.6 meV and 195 K, respectively. The inclusion of vertex corrections reduces $\Delta(0)$ to approximately 34.5 meV for the ver-FBW and 35.9 meV for the ver-FBW+ μ approach. Consequently, the critical temperature is suppressed by 11–12 K relative to the adiabatic case, yielding a T_c of 178 K for the ver-FBW and 183 K for the ver-FBW+ μ approach. These theoretical predictions are in excellent agreement with experimental measurements, which report T_c values in the range of 175–185 K for H_3S under 200 ± 5 GPa [102, 104].

This level of agreement is particularly significant given that our approach simultaneously accounts for anharmonic phonon effects, non-adiabatic e-ph vertex corrections, and the energy dependence of the DOS. Notably, we find that a one-shot evaluation of the vertex correction substantially underestimates T_c , demonstrating that iterative self-consistent calculations are essential for accurately quantifying the impact of e-ph vertex renormalization.

For comparison, we also analyze the superconducting gap using the constant DOS FSR approach. As shown in Fig. S6(a) of the Supporting Information [62], the resulting T_c values lie outside the experimentally observed range [102]. Without vertex corrections, T_c is slightly above the value obtained with FBW+ μ , while the inclusion of vertex correction leads to a strong underestimation. In Sec. VIII of the Supporting Information [62], we provide a detailed discussion of the underlying reasons for the limitations of the FSR approximation. Finally, calculations using harmonic phonons within the FBW, FBW+ μ , and FSR approaches, even when incorporating vertex corrections, tend to overestimate the T_c , as illustrated in Fig. S7(b) of the Supporting Information [62] and summarized in Table I.

Finally, recent experiments on H_3S have reported superconducting gap values from tunneling spectra, along with T_c values extracted from electrical resistance measurements [105]. Since these measurements were performed on samples at 151–161 GPa, they are not directly comparable to our calculations at 200 GPa. Nevertheless, the dimensionless BCS ratio $2\Delta(0)/k_B T_c$ provides a meaningful basis for comparison. Using the experimental

TABLE I. Electron-phonon coupling strength (λ), vertex-corrected coupling strength (λ^V), and superconducting T_c computed using adiabatic (FBW, FBW+ μ , and FSR), and vertex-corrected (ver-FBW, ver-FBW+ μ , and ver-FSR) approaches. For H₃S at 200 GPa, we use both harmonic and anharmonic phonons with a Coulomb pseudopotential $\mu_E^* = 0.16$, while for Pb we use harmonic phonons with $\mu_E^* = 0.10$. Experimental T_c values for H₃S [102–105] and Pb [106, 107] are shown for reference. All the T_c values are in K.

Material	Phonons	λ	λ^V	μ_E^*	W/o vertex correction			With vertex correction			T_c^{expt}
					T_c^{FBW}	$T_c^{\text{FBW}+\mu}$	T_c^{FSR}	$T_c^{\text{ver-FBW}}$	$T_c^{\text{ver-FBW}+\mu}$	$T_c^{\text{ver-FSR}}$	
H ₃ S	Har	2.29	1.78	0.16	235	238	246	222	226	198	175-185
	Anh	1.72	0.71	0.16	189	195	192	178	183	157	
Pb	Har	1.29	0.20	0.10	7.2	—	7.2	7.2	—	7.2	7.2

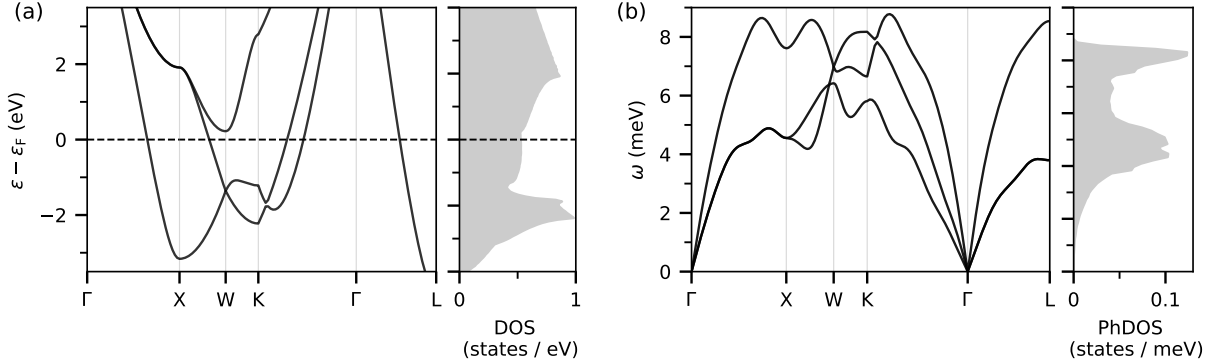


FIG. 5. (a) Electronic band structure and total DOS, and (b) phonon dispersion and PhDOS for Pb.

gap values of 29 and 32 meV with a $T_c = 190$ K for two samples at 151 and 158 GPa, the corresponding ratios are 3.54 and 3.91, respectively. As summarized in Table S1 of the Supplemental Information [62], our calculations yield ratios ranging from 4.27 to 4.55 for anharmonic cases and from 4.52 to 5.00 for harmonic ones, consistent with previous Migdal-Eliashberg results at both harmonic and anharmonic levels [58, 60]. Further theoretical calculations using different exchange-correlation functionals [108], together with experimental measurements across a broader pressure range, will be essential for resolving the difference in the BCS ratio.

D. Electronic structure and phonon dispersion of Pb

To further test our hypothesis regarding the breakdown of the Migdal approximation and the significance of e-ph vertex corrections, we analyze elemental Pb, a prototypical conventional superconductor. The electronic structure of Pb, shown in Fig. 5, features a broad band, with a nearly flat DOS around ε_F and sharp features located approximately 2 eV below and above it. The phonon spectrum extends up to ~ 9 meV and exhibits a pronounced Kohn anomaly near the W-point in the BZ, which is attributed to strong Fermi-surface nesting [109].

Although Migdal's adiabatic condition ($\hbar\omega_0/\varepsilon_F$) is well

satisfied in Pb due to the large separation between the electronic and phononic energy scales, the observed Kohn anomaly suggests the presence of nonlinear e-ph interactions [55], which are not captured by the standard treatment. These considerations motivate the inclusion of non-adiabatic e-ph vertex effects in our analysis, even for nominally conventional superconductors such as Pb.

E. Electron-phonon coupling and superconductivity with vertex correction for Pb

To investigate the e-ph interaction in Pb, we computed the isotropic Eliashberg spectral function $\alpha^2F(\omega)$ and the cumulative e-ph coupling strength $\lambda(\omega)$. As shown in Fig. 6(a), $\alpha^2F(\omega)$ exhibits a broad peak centered around 4.5 meV (transverse phonons) and a narrower peak at 8 meV (longitudinal phonons), consistent with previous reports [56, 76, 110, 111]. The total e-ph coupling strength, $\lambda=1.29$, indicates strong coupling. The high-frequency peak near 7 meV corresponds to the Kohn anomaly at the W point in the phonon dispersion, reflecting enhanced e-ph scattering from Fermi-surface nesting effects [109]. The cumulative $\lambda(\omega)$ rises sharply below 5 meV, contributing approximately 44% to the total coupling, confirming the dominant role of the low-frequency phonons in mediating Cooper pairing.

With vertex corrections, the 3D spectral function

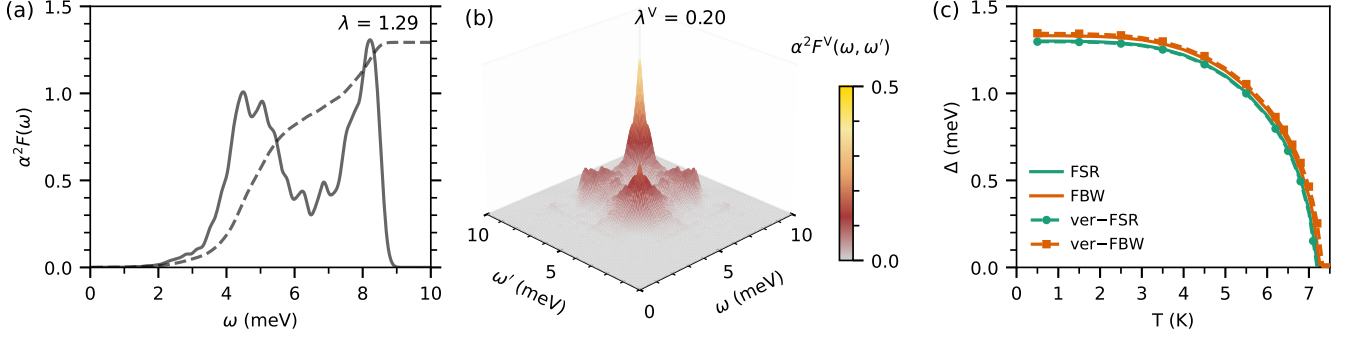


FIG. 6. (a) Eliashberg spectral function $\alpha^2 F(\omega)$ and integrated e-ph coupling constant $\lambda(\omega)$, (b) vertex-corrected Eliashberg spectral function $\alpha^2 F^V(\omega, \omega')$ and integrated vertex-corrected e-ph coupling strength λ^V , and (c) isotropic superconducting gap $\Delta(T)$ computed using the adiabatic FSR (solid teal-green), adiabatic FBW (solid orange), vertex-corrected FSR (dashed teal-green with circles), and vertex-corrected FBW (dashed orange with squares) methods for Pb.

$\alpha^2 F^V(\omega, \omega')$ (Fig. 6(b)) retains the characteristic peaks at 5 and 8 meV but yields a very low value of $\lambda^V = 0.20$, representing an 85% decrease relative to the adiabatic λ . This result confirms the validity of Migdal's approximation for Pb, where vertex corrections are negligible. We note that the e-ph coupling in Pb may be slightly enhanced by the inclusion of spin-orbit coupling, as reported in previous studies [111]; however, this effect is not expected to alter our conclusions. Additionally, the vertex-corrected tunneling inversion study by Freericks et al. [55] found that accounting for the lowest-order vertex correction altered the coupling constant by only $\sim 1\%$ and the T_c by less than 2%, further reinforcing the robustness of ME theory for conventional superconductors like Pb. While insightful, their analysis relied on additional simplifying assumptions, such as the constant DOS FSR approach with the vertex-corrected spectral function taken as the product of adiabatic kernels, which may underestimate the vertex effect.

We performed isotropic Eliashberg calculations to compute the superconducting gap $\Delta(T)$ using a Coulomb parameter $\mu_E^* = 0.1$. Figure 6(c) shows that the adiabatic FSR approach without vertex corrections yields a zero-temperature gap $\Delta(0) \approx 1.3$ meV with a gap ratio of $2\Delta(0)/k_B T_c \approx 4.3$, which exceeds the BCS weak-coupling limit and is in good agreement with the experimental $T_c \approx 7.2$ K [106, 107]. Both FSR and FBW methods produce nearly similar $\Delta(T)$ curves, reflecting the weak energy dependence of the DOS near the Fermi level and the broad electronic bandwidth of Pb. Notably, the inclusion of lowest-order vertex corrections has a negligible impact on the superconducting gap evolution. The vertex-corrected FSR and FBW results lie on top of their adiabatic counterparts across all temperatures. This insensitivity of $\Delta(0)$ and T_c to vertex corrections further validates the applicability of ME theory in describing superconductivity in adiabatic and weakly non-adiabatic systems such as Pb.

V. SUMMARY

In this work, we revisit the formulation of the lowest-order vertex corrections within the Eliashberg formalism and develop a fully *ab initio* approach to evaluate the vertex-corrected Eliashberg spectral function and the corresponding e-ph coupling strength. This methodology, implemented in the EPW code [13, 57], enables us to move beyond model Hamiltonians and apply the formalism to realistic materials such as H₃S and Pb. To solve the isotropic Eliashberg equations, we employ three approaches: the FSR, FBW with a fixed μ_F , and FBW with a self-consistently updated μ_F . For H₃S, calculations include both harmonic and anharmonic phonons using a Coulomb pseudopotential $\mu_E^* = 0.16$, while for Pb, we consider harmonic phonons with $\mu_E^* = 0.10$. In H₃S, which exhibits strong e-ph coupling, incorporating vertex corrections leads to a significant reduction in both λ and T_c , signaling a breakdown of the Migdal approximation. When effects from phonon anharmonicity and variation in the electronic DOS are taken into account, the predicted T_c agrees well with experimental measurements, resolving long-standing discrepancies between theory and experiment. By contrast, for elemental Pb, a prototypical conventional superconductor, vertex corrections have a negligible impact on both λ and T_c , consistent with the expectations of Migdal-Eliashberg theory. Overall, our findings demonstrate that vertex corrections are essential for accurately describing superconductivity in materials with strong non-adiabaticity, low carrier density, or sharp features in the DOS, such as high- T_c hydrides, while validating their negligible influence in conventional adiabatic superconductors. The computational framework established here provides a rigorous and predictive first-principles methodology for extending the applicability of Eliashberg theory beyond the conventional Migdal limit.

ACKNOWLEDGMENTS

We thank S. Tiwari and F. Giustino for insightful discussions on the numerical implementation of the vertex part in the EPW code, R. Akashi for stimulating conversations and independent verification of our derivations, and M. Zacharias for assistance with the anharmonic calculations using the ZG code. S.B.M. acknowledges H. Paudyal for early discussions on the vertex implementation. This work was primarily supported by the National Science Foundation (NSF) under Award No. DMR-2035518. Part of this research was supported by the NSF, Office of Advanced Cyberinfrastructure under Grant No. 2103991 of the Cyberinfrastructure for Sustained Scientific (parallelization of the isotropic superconductivity module). Computational resources were provided by the

Frontera and Stampede3 supercomputers at the Texas Advanced Computing Center (TACC) at The University of Texas at Austin (<http://www.tacc.utexas.edu>), supported through the Leadership Resource Allocation (LRAC) award DMR22004 and the ACCESS allocation TG-DMR180071, respectively.

AUTHOR CONTRIBUTIONS

R.M. conceived the ideas and secured the funding. R.M. and S.M. derived the theory. S.M. implemented the vertex correction in the EPW code in consultation with H.M. S.M. performed the calculations and drafted the manuscript. R.M. supervised the project and revised the manuscript. All authors were involved in the formal analysis and participated in the review and editing of the final manuscript.

-
- [1] A. B. Migdal, Interaction between electrons and lattice vibrations in a normal metal, *Sov. Phys. JETP* **7**, 996 (1958).
 - [2] G. Eliashberg, Interactions between electrons and lattice vibrations in a superconductor, *Sov. Phys. JETP* **11**, 696 (1960).
 - [3] G. M. Eliashberg, Temperature Green's function for electrons in a superconductor, *Sov. Phys. JETP* **12**, 1000 (1961).
 - [4] J. P. Carbotte, Properties of boson-exchange superconductors, *Rev. Mod. Phys.* **62**, 1027 (1990).
 - [5] D. J. Scalapino, J. R. Schrieffer, and J. W. Wilkins, Strong-Coupling Superconductivity. I, *Phys. Rev.* **148**, 263 (1966).
 - [6] D. J. Scalapino, The electron-phonon interaction and strong-coupling superconductors, edited by R. D. Parks, in *Superconductivity*, Vol. 1 (Dekker, 1969) pp. 449–560.
 - [7] W. E. Pickett, Generalization of the theory of the electron-phonon interaction: Thermodynamic formulation of superconducting- and normal-state properties, *Phys. Rev. B* **26**, 1186 (1982).
 - [8] P. B. Allen and B. Mitrović, Theory of Superconducting T_c (Academic Press, 1983) pp. 1–92.
 - [9] F. Marsiglio and J. Carbotte, Electron-phonon superconductivity, in *Superconductivity: conventional and unconventional superconductors* (Springer Berlin Heidelberg, 2008) pp. 73–162.
 - [10] F. Marsiglio, Eliashberg theory: A short review, *Annals of Physics* **417**, 168102 (2020).
 - [11] W. E. Pickett, Colloquium: Room temperature superconductivity: The roles of theory and materials design, *Rev. Mod. Phys.* **95**, 021001 (2023).
 - [12] J. Bardeen, L. N. Cooper, and J. R. Schrieffer, Theory of superconductivity, *Phys. Rev.* **108**, 1175 (1957).
 - [13] S. Poncé, E. Margine, C. Verdi, and F. Giustino, EPW: Electron-phonon coupling, transport and superconducting properties using maximally localized Wannier functions, *Comput. Phys. Commun.* **209**, 116 (2016).
 - [14] A. Sanna, C. Pellegrini, and E. K. U. Gross, Combining eliashberg theory with density functional theory for the accurate prediction of superconducting transition temperatures and gap functions, *Phys. Rev. Lett.* **125**, 057001 (2020).
 - [15] G. Marini, G. Marchese, G. Profeta, J. Sjakste, F. Macheda, N. Vast, F. Mauri, and M. Calandra, EPIQ: An open-source software for the calculation of electron-phonon interaction related properties, *Comp. Phys. Comm.* **295**, 108950 (2024).
 - [16] M. A. L. Marques, M. Lüdgers, N. N. Lathiotakis, G. Profeta, A. Floris, L. Fast, A. Continenza, E. K. U. Gross, and S. Massidda, Ab initio theory of superconductivity. ii. application to elemental metals, *Phys. Rev. B* **72**, 024546 (2005).
 - [17] R. Arita, T. Koretsune, S. Sakai, R. Akashi, Y. Nomura, and W. Sano, Nonempirical Calculation of Superconducting Transition Temperatures in Light-Element Superconductors, *Adv. Mater.* **29**, 1602421 (2017).
 - [18] A. Sanna, J. A. Flores-Livas, A. Davydov, G. Profeta, K. Dewhurst, S. Sharma, and E. K. U. Gross, Ab initio Eliashberg Theory: Making Genuine Predictions of Superconducting Features, *J. Phys. Soc. Jpn.* **87**, 041012 (2018).
 - [19] A. Davydov, A. Sanna, C. Pellegrini, J. K. Dewhurst, S. Sharma, and E. K. U. Gross, Ab initio theory of plasmonic superconductivity within the Eliashberg and density-functional formalisms, *Phys. Rev. B* **102**, 214508 (2020).
 - [20] J. A. Flores-Livas, A. Sanna, and E. Gross, High temperature superconductivity in sulfur and selenium hydrides at high pressure, *Eur. Phys. J. B* **89**, 1 (2016).
 - [21] C. Pellegrini and A. Sanna, Ab initio methods for superconductivity, *Nat. Rev. Phys.* **6**, 509 (2024).
 - [22] M. Born and R. Oppenheimer, Zur quantentheorie der molekeln, *Annalen der Physik* **389**, 457 (1927).
 - [23] T. Jarlborg and A. Bianconi, Breakdown of the Migdal approximation at Lifshitz transitions with giant zero-point motion in the H₃S superconductor, *Sci. Rep.* **6**, 24816 (2016).
 - [24] W. Sano, T. Koretsune, T. Tadano, R. Akashi, and R. Arita, Effect of Van Hove singularities on high- T_c su-

- perconductivity in H_3S , *Phys. Rev. B* **93**, 094525 (2016).
- [25] A. P. Durajski and R. Szczesniak, Migdal-Eliashberg equations - the effective model for superconducting state in H_3S , [arXiv:1609.06079](#) (2016).
- [26] L. P. Gor'kov and V. Z. Kresin, Pressure and high- T_c superconductivity in sulfur hydrides, *Sci. Rep.* **6**, 25608 (2016).
- [27] L. P. Gor'kov and V. Z. Kresin, Colloquium: High pressure and road to room temperature superconductivity, *Rev. Mod. Phys.* **90**, 011001 (2018).
- [28] B. Roy, J. D. Sau, and S. Das Sarma, Migdal's theorem and electron-phonon vertex corrections in Dirac materials, *Phys. Rev. B* **89**, 165119 (2014).
- [29] O. Gunnarsson, V. Meden, and K. Schönhammer, Corrections to migdal's theorem for spectral functions: A cumulant treatment of the time-dependent green's function, *Phys. Rev. B* **50**, 10462 (1994).
- [30] E. Cappelluti, C. Grimaldi, L. Pietronero, and S. Strässler, Nonadiabatic Channels in the Superconducting Pairing of Fullerides, *Phys. Rev. Lett.* **85**, 4771 (2000).
- [31] M. N. Gastiasoro, A. V. Chubukov, and R. M. Fernandes, Phonon-mediated superconductivity in low carrier-density systems, *Phys. Rev. B* **99**, 094524 (2019).
- [32] S.-Q. Hu, X.-B. Liu, D.-Q. Chen, C. Lian, E.-G. Wang, and S. Meng, Nonadiabatic electron-phonon coupling and its effects on superconductivity, *Phys. Rev. B* **105**, 224311 (2022).
- [33] L. P. Gor'kov, Superconducting transition temperature: Interacting fermi gas and phonon mechanisms in the nonadiabatic regime, *Phys. Rev. B* **93**, 054517 (2016).
- [34] S.-S. Zhang, Z. M. Raines, and A. V. Chubukov, Applicability of eliashberg theory for systems with electron-phonon and electron-electron interaction: A comparative analysis, *Phys. Rev. B* **109**, 245132 (2024).
- [35] L. Pietronero and S. Strässler, Theory of nonadiabatic superconductivity, *Europhys. Lett.* **18**, 627 (1992).
- [36] Kostur, Vladimir N. and Mitrović, Božidar, Electron-phonon interaction in two dimensions: Variation of $\text{Im}\Sigma(\epsilon_p, \omega)$ with increasing ω_D/E_F , *Phys. Rev. B* **48**, 16388 (1993).
- [37] Kostur, Vladimir N. and Mitrović, Božidar, Calculations of the superconducting critical temperature with vertex corrections, *Phys. Rev. B* **50**, 12774 (1994).
- [38] C. Grimaldi, L. Pietronero, and S. Strässler, Nonadiabatic Superconductivity: Electron-Phonon Interaction Beyond Migdal's Theorem, *Phys. Rev. Lett.* **75**, 1158 (1995).
- [39] L. Pietronero, S. Strässler, and C. Grimaldi, Nonadiabatic superconductivity. I. Vertex corrections for the electron-phonon interactions, *Phys. Rev. B* **52**, 10516 (1995).
- [40] C. Grimaldi, L. Pietronero, and S. Strässler, Nonadiabatic superconductivity. II. Generalized Eliashberg equations beyond Migdal's theorem, *Phys. Rev. B* **52**, 10530 (1995).
- [41] M. Botti, E. Cappelluti, C. Grimaldi, and L. Pietronero, Nonadiabatic theory of the superconducting state, *Phys. Rev. B* **66**, 054532 (2002).
- [42] L. Pietronero and E. Cappelluti, Nonadiabatic breakdown and pairing in high- T_c compounds, *Low Temp. Phys.* **32**, 340 (2006).
- [43] V. Velasco, G. Midei, M. Capone, and A. Perali, Pairing amplification induced by nonadiabatic effects on the electron-phonon interaction throughout the BCS-BEC crossover, *Phys. Rev. B* **111**, 064512 (2025).
- [44] I. Esterlis, B. Nosarzewski, E. W. Huang, B. Moritz, T. P. Devereaux, D. J. Scalapino, and S. A. Kivelson, Breakdown of the Migdal-Eliashberg theory: A determinant quantum Monte Carlo study, *Phys. Rev. B* **97**, 140501 (2018).
- [45] A. S. Alexandrov, Breakdown of the migdal-eliashberg theory in the strong-coupling adiabatic regime, *Europhys. Lett.* **56**, 92 (2001).
- [46] A. V. Chubukov, A. Abanov, I. Esterlis, and S. A. Kivelson, Eliashberg theory of phonon-mediated superconductivity — when it is valid and how it breaks down, *Annals of Physics* **417**, 168190 (2020).
- [47] E. Cappelluti, C. Grimaldi, and L. Pietronero, Electron-phonon driven unconventional superconductivity: The role of small fermi energies and of nonadiabatic processes, *Physica C: Supercond.* **613**, 1354343 (2023).
- [48] F. Schrodi, P. M. Oppeneer, and A. Aperis, Full-bandwidth Eliashberg theory of superconductivity beyond Migdal's approximation, *Phys. Rev. B* **102**, 024503 (2020).
- [49] N.-E. Lee, J.-J. Zhou, H.-Y. Chen, and M. Bernardi, Ab initio electron-two-phonon scattering in GaAs from next-to-leading order perturbation theory, *Nat. Commun.* **11**, 1607 (2020).
- [50] R. Bianco and I. Errea, Non-perturbative theory of the electron-phonon coupling and its first-principles implementation, [arXiv:2303.02621](#) (2023).
- [51] M. Houtput, L. Ranalli, C. Verdi, S. Klimin, S. Ragni, C. Franchini, and J. Tempere, First-principles theory of nonlinear long-range electron-phonon interaction, *Phys. Rev. B* **111**, 184320 (2025).
- [52] I. Zappacosta, M. Houtput, and J. Tempere, Nonlinear electron-phonon interactions in the Migdal-Eliashberg theory, *Phys. Rev. B* **111**, 214525 (2025).
- [53] J.-M. Lihm and S. Poncé, Nonperturbative self-consistent electron-phonon spectral functions and transport, *Phys. Rev. Lett.* **134**, 186401 (2025).
- [54] J.-M. Lihm and S. Poncé, Beyond-quasiparticles transport with vertex correction: self-consistent ladder formalism for electron-phonon interactions, [arXiv:2506.18139](#) (2025).
- [55] J. K. Freericks, E. J. Nicol, A. Y. Liu, and A. A. Quong, Vertex-corrected tunneling inversion in electron-phonon mediated superconductors: Pb, *Phys. Rev. B* **55**, 11651 (1997).
- [56] E. R. Margine and F. Giustino, Anisotropic Migdal-Eliashberg theory using Wannier functions, *Phys. Rev. B* **87**, 024505 (2013).
- [57] H. Lee, S. Poncé, K. Bushick, S. Hajinazar, J. Lafuente-Bartolome, J. Leveillee, C. Lian, J.-M. Lihm, F. Macheda, H. Mori, H. Paudyal, W. H. Sio, S. Tiwari, M. Zacharias, X. Zhang, N. Bonini, E. Kioupakis, E. R. Margine, and F. Giustino, Electron-phonon physics from first principles using the EPW code, *npj Comput. Mater.* **9**, 2057 (2023).
- [58] R. Lucrezi, P. P. Ferreira, S. Hajinazar, H. Mori, H. Paudyal, E. R. Margine, and C. Heil, Full-bandwidth anisotropic Migdal-Eliashberg theory and its application to superhydrides, *Commun. Phys.* **7**, 33 (2024).
- [59] K. P. Hilleke and E. Zurek, Tuning chemical precompression: Theoretical design and crystal chemistry of novel hydrides in the quest for warm and light super-

- conductivity at ambient pressures, *J. Appl. Phys.* **131**, 070901 (2022).
- [60] I. Errea, M. Calandra, C. J. Pickard, J. Nelson, R. J. Needs, Y. Li, H. Liu, Y. Zhang, Y. Ma, and F. Mauri, High-pressure hydrogen sulfide from first principles: A strongly anharmonic phonon-mediated superconductor, *Phys. Rev. Lett.* **114**, 157004 (2015).
- [61] R. Taureau, M. Cherubini, T. Morresi, and M. Casula, Quantum symmetrization transition in superconducting sulfur hydride from quantum Monte Carlo and path integral molecular dynamics, *npj Comput. Mater.* **10**, 56 (2024).
- [62] See Supplemental Material for additional information. In Sec. I, we provide a detailed diagrammatic analysis of the electron self-energy. In Secs. II–VI, we derive the isotropic adiabatic and vertex-corrected Eliashberg equations, including their simplifications and Matsubara summation procedures. Sections VII present convergence tests for harmonic and anharmonic phonons, and Sec. VIII describes superconducting properties with vertex corrections for H₃S at 200 GPa. Figure S1 illustrates the Feynman diagrams contributing to the electron self-energy, along with schematic representations of the associated Fermi-surface scattering processes. Figure S2 shows the sign convention for the Levi-Civita symbol ϵ_{ijk} based on cyclic permutations. Figure S3 presents the convergence of the harmonic phonon spectra of H₃S with respect to the \mathbf{q} -point grid and the kinetic energy cutoff. Figure S4 justifies the use of a coarser \mathbf{k} -mesh ($12 \times 12 \times 12$) for anharmonic calculations in H₃S and examines the effect of varying the displacement amplitude from 0.01 Å to 0.2 Å. Figure S5 shows the convergence of the anharmonic phonon spectra of H₃S with respect to supercell size and iterative self-consistency, achieved using a linear mixing scheme. Figure S6 presents the superconducting gap in H₃S computed using the FSR, FBW, and FBW+ μ approaches with harmonic and anharmonic phonons, both with and without vertex corrections. Table S1 summarizes superconducting properties of H₃S computed in this study.
- [63] Y. Nambu, Quasi-particles and gauge invariance in the theory of superconductivity, *Phys. Rev.* **117**, 648 (1960).
- [64] M. Zacharias, G. Volonakis, F. Giustino, and J. Even, Anharmonic lattice dynamics via the special displacement method, *Phys. Rev. B* **108**, 035155 (2023).
- [65] R. Heid, Relevance of quadratic electron-phonon coupling for the superconducting transition temperature, *Phys. Rev. B* **45**, 5052 (1992).
- [66] P. M. Dee, J. Coulter, K. G. Kleiner, and S. Johnston, Relative importance of nonlinear electron-phonon coupling and vertex corrections in the Holstein model, *Comm. Phys.* **3**, 145 (2020).
- [67] F. Giustino, M. L. Cohen, and S. G. Louie, Electron-phonon interaction using Wannier functions, *Phys. Rev. B* **76**, 165108 (2007).
- [68] F. Giustino, Electron-phonon interactions from first principles, *Rev. Mod. Phys.* **89**, 015003 (2017).
- [69] S. Baroni, S. de Gironcoli, A. Dal Corso, and P. Giannozzi, Phonons and related crystal properties from density-functional perturbation theory, *Rev. Mod. Phys.* **73**, 515 (2001).
- [70] L. Gor'Kov, On the energy spectrum of superconductors, *Sov. Phys. JETP* **7**, 158 (1958).
- [71] J. R. Schrieffer, Theory of superconductivity (CRC Press, 1999).
- [72] G. D. Mahan, Many-particle physics (Plenum, New York, 1993).
- [73] L. Hedin, New Method for Calculating the One-Particle Green's Function with Application to the Electron-Gas Problem, *Phys. Rev.* **139**, A796 (1965).
- [74] M. S. Hybertsen and S. G. Louie, Electron correlation in semiconductors and insulators: Band gaps and quasiparticle energies, *Phys. Rev. B* **34**, 5390 (1986).
- [75] C. Pellegrini, C. Kukkonen, and A. Sanna, Ab initio calculations of superconducting transition temperatures: When going beyond RPA is essential, *Phys. Rev. B* **108**, 064511 (2023).
- [76] H. Mori, T. Nomoto, R. Arita, and E. R. Margine, Efficient anisotropic Migdal-Eliashberg calculations with an intermediate representation basis and Wannier interpolation, *Phys. Rev. B* **110**, 064505 (2024).
- [77] E. Kogler, D. Spath, R. Lucrezi, H. Mori, Z. Zhu, Z. Li, E. R. Margine, and C. Heil, IsoME: Streamlining High-Precision Eliashberg Calculations, [arXiv:2503.03559](https://arxiv.org/abs/2503.03559) (2025).
- [78] P. Morel and P. W. Anderson, Calculation of the superconducting state parameters with retarded electron-phonon interaction, *Phys. Rev.* **125**, 1263 (1962).
- [79] P. B. Allen and R. C. Dynes, Transition temperature of strong-coupled superconductors reanalyzed, *Phys. Rev. B* **12**, 905 (1975).
- [80] E. Cappelluti and L. Pietronero, Electron-phonon interaction and breakdown of the adiabatic principle in fullerenes and MgB₂, *J. Phys. Chem. Solids* **67**, 1941 (2006).
- [81] R. Heid, Electron-phonon coupling, Lecture Notes of the Autumn School on Correlated Electrons; Pavarini, E., Koch, E., Scalettar, R., Martin, R., Eds, 399 (2017).
- [82] P. Szabó, P. Samuely, J. Kačmarčík, T. Klein, J. Marcus, D. Fruchart, S. Miraglia, C. Marcenat, and A. G. M. Jansen, Evidence for two superconducting energy gaps in MgB₂ by point-contact spectroscopy, *Phys. Rev. Lett.* **87**, 137005 (2001).
- [83] C. R. Tomassetti, G. P. Kaffé, E. T. Marcial, E. R. Margine, and A. N. Kolmogorov, Prospect of high-temperature superconductivity in layered metal borocarbides, *J. Mater. Chem. C* **12**, 4870 (2024).
- [84] E. Margine, H. Lambert, and F. Giustino, Electron-phonon interaction and pairing mechanism in superconducting Ca-intercalated bilayer graphene, *Sci. Rep.* **6**, 21414 (2016).
- [85] S. B. Mishra, E. T. Marcial, S. Debata, A. N. Kolmogorov, and E. R. Margine, Stability-superconductivity map for compressed Na-intercalated graphite, *Phys. Rev. B* **110**, 174508 (2024).
- [86] C. Heil, S. Poncé, H. Lambert, M. Schlipf, E. R. Margine, and F. Giustino, Origin of Superconductivity and Latent Charge Density Wave in NbS₂, *Phys. Rev. Lett.* **119**, 087003 (2017).
- [87] S. Das, H. Paudyal, E. R. Margine, D. F. Agterberg, and I. I. Mazin, Electron-phonon coupling and spin fluctuations in the Ising superconductor NbSe₂, *npj Computational Materials* **9**, 66 (2023).
- [88] P. Giannozzi, O. Andreussi, T. Brumme, O. Bunau, M. Buongiorno Nardelli, M. Calandra, R. Car, C. Cavazzoni, D. Ceresoli, M. Cococcioni, N. Colonna, I. Carnimeo, A. Dal Corso, S. de Gironcoli, P. Delu-

- gas, R. A. DiStasio Jr, A. Ferretti, A. Floris, G. Fratesi, G. Fugallo, R. Gebauer, U. Gerstmann, F. Giustino, T. Gorni, J. Jia, M. Kawamura, H. Y. Ko, A. Kokalj, E. Küçükbenli, M. Lazzeri, M. Marsili, N. Marzari, F. Mauri, N. L. Nguyen, H.-V. Nguyen, A. Otero-de-la Roza, L. Paulatto, S. Poncé, D. Rocca, R. Sabatini, B. Santra, M. Schlipf, A. P. Seitsonen, A. Smogunov, I. Timrov, T. Thonhauser, P. Umari, N. Vast, X. Wu, and S. Baroni, Advanced capabilities for materials modelling with Quantum ESPRESSO, *J. Phys.: Condens. Matter* **29**, 465901 (2017).
- [89] D. R. Hamann, Optimized norm-conserving Vanderbilt pseudopotentials, *Phys. Rev. B* **88**, 085117 (2013).
- [90] J. P. Perdew, K. Burke, and M. Ernzerhof, Generalized gradient approximation made simple, *Phys. Rev. Lett.* **77**, 3865 (1996).
- [91] M. Methfessel and A. T. Paxton, High-precision sampling for Brillouin-zone integration in metals, *Phys. Rev. B* **40**, 3616 (1989).
- [92] M. Zacharias and F. Giustino, Theory of the special displacement method for electronic structure calculations at finite temperature, *Phys. Rev. Res.* **2** (2020).
- [93] N. Marzari, A. A. Mostofi, J. R. Yates, I. Souza, and D. Vanderbilt, Maximally localized Wannier functions: Theory and applications, *Rev. Mod. Phys.* **84**, 1419 (2012).
- [94] G. Pizzi, V. Vitale, R. Arita, S. Blügel, F. Freimuth, G. Géranton, M. Gibertini, D. Gresch, C. Johnson, T. Koretsune, J. Ibañez-Azpiroz, H. Lee, J.-M. Lihm, D. Marchand, A. Marrazzo, Y. Mokrousov, J. I. Mustafa, Y. Nohara, Y. Nomura, L. Paulatto, S. Poncé, T. Ponweiser, J. Qiao, F. Thöle, S. S. Tsirkin, M. Wierzbowska, N. Marzari, D. Vanderbilt, I. Souza, A. A. Mostofi, and J. R. Yates, Wannier90 as a community code: new features and applications, *J. Phys. Condens. Matter* **32**, 165902 (2020).
- [95] A. Marrazzo, S. Beck, E. R. Margine, N. Marzari, A. A. Mostofi, J. Qiao, I. Souza, S. S. Tsirkin, J. R. Yates, and G. Pizzi, Wannier-function software ecosystem for materials simulations, *Rev. Mod. Phys.* **96**, 045008 (2024).
- [96] D. Duan, Y. Liu, F. Tian, D. Li, X. Huang, Z. Zhao, H. Yu, B. Liu, W. Tian, and T. Cui, Pressure-induced metallization of dense $(\text{H}_2\text{S})_2\text{H}_2$ with high- T_c superconductivity, *Sci. Rep.* **4**, 6968 (2014).
- [97] N. Bernstein, C. S. Hellberg, M. D. Johannes, I. I. Mazin, and M. J. Mehl, What superconducts in sulfur hydrides under pressure and why, *Phys. Rev. B* **91**, 060511 (2015).
- [98] Y. Quan and W. E. Pickett, Van Hove singularities and spectral smearing in high-temperature superconducting H_3S , *Phys. Rev. B* **93**, 104526 (2016).
- [99] R. Akashi, Archetypical “push the band critical point” mechanism for peaking of the density of states in three-dimensional crystals: Theory and case study of cubic H_3S , *Phys. Rev. B* **101**, 075126 (2020).
- [100] S. R. Thomsen and M. G. Goesten, Symmetry-Shaped Singularities in High-Temperature Superconductor H_3S , *J. Am. Chem. Soc.* **146**, 18298 (2024).
- [101] R. Akashi, M. Kawamura, S. Tsuneyuki, Y. Nomura, and R. Arita, First-principles study of the pressure and crystal-structure dependences of the superconducting transition temperature in compressed sulfur hydrides, *Phys. Rev. B* **91**, 224513 (2015).
- [102] A. P. Drozdov, M. I. Eremets, I. A. Troyan, V. Ksenofontov, and S. I. Shylin, Conventional superconductivity at 203 kelvin at high pressures in the sulfur hydride system, *Nature* **525**, 73 (2015).
- [103] M. Einaga, M. Sakata, T. Ishikawa, K. Shimizu, M. I. Eremets, A. P. Drozdov, I. A. Troyan, N. Hirao, and Y. Ohishi, Crystal structure of the superconducting phase of sulfur hydride, *Nature physics* **12**, 835 (2016).
- [104] H. Nakao, M. Einaga, M. Sakata, M. Kitagaki, K. Shimizu, S. Kawaguchi, N. Hirao, and Y. Ohishi, Superconductivity of pure H_3S synthesized from elemental sulfur and hydrogen, *J. Phys. Soc. Jpn.* **88**, 123701 (2019).
- [105] F. Du, A. P. Drozdov, V. S. Minkov, F. F. Balakirev, P. Kong, G. A. Smith, J. Yan, B. Shen, P. Gegenwart, and M. I. Eremets, Superconducting gap of H_3S measured by tunnelling spectroscopy, *Nature* **641**, 619–624 (2025).
- [106] P. Townsend and J. Sutton, Investigation by Electron Tunneling of the Superconducting Energy Gaps in Nb, Ta, Sn, and Pb, *Phys. Rev.* **128**, 591 (1962).
- [107] R. Khasanov, D. Das, D. J. Gawryluk, R. Gupta, and C. Mielke, Isotropic single-gap superconductivity of elemental pb, *Phys. Rev. B* **104**, L100508 (2021).
- [108] Y. Wang, M. Engel, C. Lane, H. Miranda, L. Hou, B. Barbiellini, R. S. Markiewicz, J.-X. Zhu, G. Kresse, A. Bansil, J. Sun, and R. Zhang, Accurate Electron-phonon Interactions from Advanced Density Functional Theory, *arXiv:2411.08192* (2024).
- [109] P. Aynajian, T. Keller, L. Boeri, S. Shapiro, K. Habicht, and B. Keimer, Energy gaps and kohn anomalies in elemental superconductors, *Science* **319**, 1509 (2008).
- [110] A. Y. Liu and A. A. Quong, Linear-response calculation of electron-phonon coupling parameters, *Phys. Rev. B* **53**, R7575 (1996).
- [111] R. Heid, K.-P. Bohnen, I. Y. Sklyadneva, and E. V. Chulkov, Effect of spin-orbit coupling on the electron-phonon interaction of the superconductors Pb and Tl, *Phys. Rev. B* **81**, 174527 (2010).

Supporting Information:

Electron-phonon vertex correction effect in superconducting H₃S

Shashi B. Mishra,^{1,*} Hitoshi Mori,^{1,2} and Elena R. Margine^{1,†}

¹*Department of Physics, Applied Physics and Astronomy,
Binghamton University-SUNY, Binghamton, New York 13902, USA*

²*Institute for Materials Research, Tohoku University, Sendai 980-8577, Japan*
(Dated: July 16, 2025)

CONTENTS

	1
I. Diagrammatic representation of the electron-phonon self-energy	2
II. Derivation of the isotropic self-energy expression	3
III. Symmetry reduction of the vertex-corrected Eliashberg spectral function	5
IV. Simplification of the vertex-corrected self-energy within Eliashberg formalism	5
V. Summation procedure over Matsubara frequencies	7
VI. Derivation of the isotropic Fermi-surface restricted expressions	8
VII. Convergence of harmonic and anharmonic phonon calculations for H ₃ S	9
VIII. Superconducting properties with vertex corrections for H ₃ S	11
References	12

I. DIAGRAMMATIC REPRESENTATION OF THE ELECTRON-PHONON SELF-ENERGY

Figure S1 presents several lowest-order Feynman diagrams contributing to the electron self-energy, including the standard non-crossing Migdal diagram [1], and their corresponding scattering processes on the Fermi surface. Diagrams (b) and (c) depict next-order corrections to the Migdal diagram, while (d) represents the lowest-order vertex correction that accounts for scattering between multiple intermediate states beyond the Migdal approximation [2]. The right panels (e-h) illustrate schematically the associated Fermi surface scattering processes, where arrows indicate the momentum transfer between the electronic states. The diagrams in (f) and (g) demonstrate that these processes are largely confined near the Fermi surface and, as discussed in several Refs. [2-4], lead to small energy shifts that are effectively summed in the Migdal approximation. In contrast, the vertex correction (d) and its associated scattering pathway in (h) involve off-shell intermediate states. These processes, typically neglected in Migdal theory, become increasingly important in systems exhibiting strong non-adiabatic effects or enhanced Fermi-surface nesting.

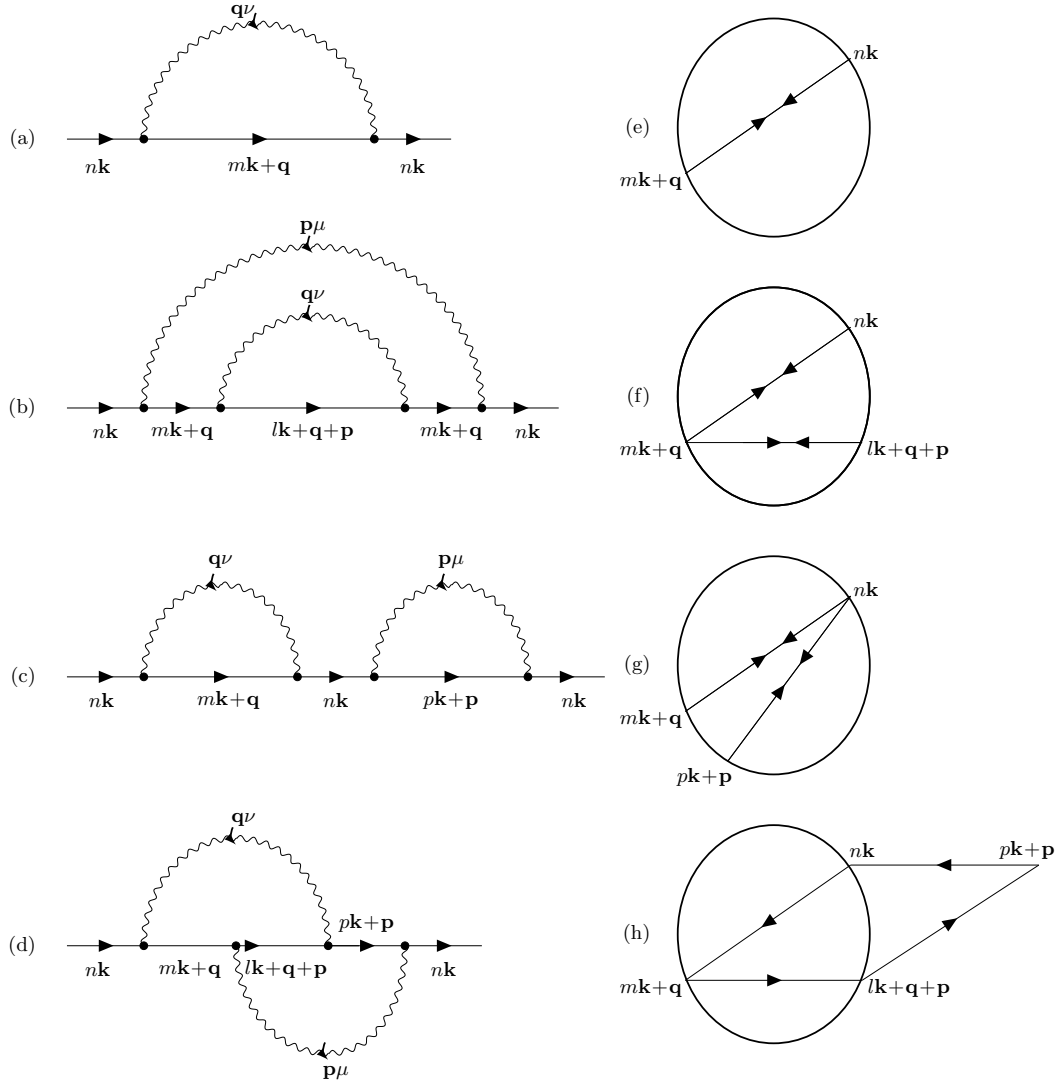


FIG. S1. (a-d) Feynman diagrams illustrating the lowest-order electron self-energy contributions, corresponding to Fig. 1(b) in the main text. (e-h) Schematic representations of the associated Fermi surfaces and electronic states involved in the respective scattering processes. Panel (a) depicts the standard Migdal diagram, while panels (b) and (c) show next-order self-energy corrections, whose effects are effectively included in (a). The corresponding scattering processes are shown in (e) and (f), respectively. Panel (d) illustrates the lowest-order vertex correction, with the corresponding scattering representation given in (h).

II. DERIVATION OF THE ISOTROPIC SELF-ENERGY EXPRESSION

The self-energy expression given by Eq. (17) of the main text couples electronic states with momenta \mathbf{k} . To derive the isotropic equations, we simplify the $n\mathbf{k}$ -dependence by defining the energy-resolved average of a quantity $A_{n\mathbf{k}}$ as [5]

$$A(\varepsilon) = \frac{\sum_{n\mathbf{k}} A_{n\mathbf{k}} \delta(\varepsilon_{n\mathbf{k}} - \varepsilon)}{\sum_{n\mathbf{k}} \delta(\varepsilon_{n\mathbf{k}} - \varepsilon)} = \frac{\sum_{n\mathbf{k}} A_{n\mathbf{k}} \delta(\varepsilon_{n\mathbf{k}} - \varepsilon)}{N(\varepsilon)}. \quad (1)$$

Here, $N(\varepsilon) = \sum_{n\mathbf{k}} \delta(\varepsilon_{n\mathbf{k}} - \varepsilon)$ denotes the electronic density of states (DOS) per spin at energy ε .

Using Eq. (1), the isotropic form of adiabatic self-energy $\hat{\Sigma}_{n\mathbf{k}}^{(A)}(i\omega_j)$ from Eq. (22) of the main text simplifies to

$$\begin{aligned} \hat{\Sigma}^{(A)}(\varepsilon, i\omega_j) &= \frac{1}{N(\varepsilon)} \sum_{n\mathbf{k}} \hat{\Sigma}_{n\mathbf{k}}^{(A)}(i\omega_j) \delta(\varepsilon_{n\mathbf{k}} - \varepsilon) \\ &= \frac{k_B T}{N(\varepsilon)} \sum_{nm} \sum_{\mathbf{kq}} \sum_{j'} \frac{\lambda_{n\mathbf{k}, m\mathbf{k}+\mathbf{q}}(i\omega_j - i\omega_{j'})}{N_F} \delta(\varepsilon_{n\mathbf{k}} - \varepsilon) \hat{\tau}_3 \hat{G}_{m\mathbf{k}+\mathbf{q}}(i\omega_{j'}) \hat{\tau}_3. \end{aligned} \quad (2)$$

To express this in terms of energy-resolved quantities, we insert the identity $\int_{-\infty}^{+\infty} d\varepsilon' \delta(\varepsilon_{m\mathbf{k}+\mathbf{q}} - \varepsilon') = 1$ into the right-hand side (RHS) of Eq. (2), leading to

$$\begin{aligned} \hat{\Sigma}^{(A)}(\varepsilon, i\omega_j) &= \frac{k_B T}{N_F} \int_{-\infty}^{+\infty} d\varepsilon' \frac{1}{N(\varepsilon)} \sum_{nm} \sum_{\mathbf{kq}} \sum_{j'} \lambda_{n\mathbf{k}, m\mathbf{k}+\mathbf{q}}(i\omega_j - i\omega_{j'}) \delta(\varepsilon_{n\mathbf{k}} - \varepsilon) \delta(\varepsilon_{m\mathbf{k}+\mathbf{q}} - \varepsilon') \hat{\tau}_3 \hat{G}_{m\mathbf{k}+\mathbf{q}}(i\omega_{j'}) \hat{\tau}_3 \\ &= \frac{k_B T}{N_F} \int_{-\infty}^{+\infty} d\varepsilon' \frac{N(\varepsilon')}{N(\varepsilon)N(\varepsilon')} \sum_{nm} \sum_{\mathbf{kq}} \sum_{j'} \lambda_{n\mathbf{k}, m\mathbf{k}+\mathbf{q}}(i\omega_j - i\omega_{j'}) \delta(\varepsilon_{n\mathbf{k}} - \varepsilon) \delta(\varepsilon_{m\mathbf{k}+\mathbf{q}} - \varepsilon') \hat{\tau}_3 \hat{G}_{m\mathbf{k}+\mathbf{q}}(i\omega_{j'}) \hat{\tau}_3. \end{aligned} \quad (3)$$

In the second line of Eq. (3), we have inserted the factor $\frac{N(\varepsilon')}{N(\varepsilon)}$ to facilitate simplification. To proceed, we define a double average over \mathbf{k} and $\mathbf{k} + \mathbf{q}$ on the RHS of Eq. (3) as follows

$$\frac{1}{N(\varepsilon)N(\varepsilon')} \sum_{nm} \sum_{\mathbf{kq}} \lambda_{n\mathbf{k}, m\mathbf{k}+\mathbf{q}}(i\omega_j - i\omega_{j'}) \hat{G}_{m\mathbf{k}+\mathbf{q}}(i\omega_{j'}) \delta(\varepsilon_{n\mathbf{k}} - \varepsilon) \delta(\varepsilon_{m\mathbf{k}+\mathbf{q}} - \varepsilon') \approx \lambda(\varepsilon, \varepsilon', i\omega_j - i\omega_{j'}) \hat{G}(\varepsilon', i\omega_{j'}). \quad (4)$$

This approximation allows us to decouple the integration over the electron-phonon (e-ph) kernel and the electron Green's function in the energy domain. Following Allen and Mitrović [2], we neglect the energy dependence of the e-ph kernel $\lambda(\varepsilon, \varepsilon', i\omega_j - i\omega_{j'})$ and evaluate it at the Fermi level:

$$\lambda(\varepsilon, \varepsilon', i\omega_j - i\omega_{j'}) \approx \lambda(\varepsilon_F, \varepsilon_F, i\omega_j - i\omega_{j'}) \equiv \lambda(i\omega_j - i\omega_{j'}). \quad (5)$$

This approximation is justified by the assumption that only electronic states near Fermi level (ε_F) contribute significantly to the e-ph interaction; that is, $\delta(\varepsilon_{n\mathbf{k}} - \varepsilon) \rightarrow \delta(\varepsilon_{n\mathbf{k}} - \varepsilon_F)$. Furthermore, the \mathbf{k} -dependence of the Green's function $\hat{G}_{n\mathbf{k}}(i\omega_j)$ (see Eq. (11) in the main text) enters through the band energy $\varepsilon_{n\mathbf{k}}$. Thus, the dominant ε' dependence of the energy-resolved Green's function $\hat{G}(\varepsilon', i\omega_{j'})$ arises from the explicit appearance of ε' .

Substituting these approximations into Eq. (3), we obtain the isotropic adiabatic self-energy:

$$\hat{\Sigma}^{(A)}(i\omega_j) = \frac{k_B T}{N_F} \sum_{j'} \lambda(i\omega_j - i\omega_{j'}) \int_{-\infty}^{+\infty} d\varepsilon' N(\varepsilon') \hat{\tau}_3 \hat{G}(\varepsilon', i\omega_{j'}) \hat{\tau}_3. \quad (6)$$

Here, the isotropic e-ph kernel $\lambda(i\omega_j - i\omega_{j'})$ is defined as

$$\begin{aligned} \lambda(i\omega_j - i\omega_{j'}) &= \frac{\sum_{nm} \sum_{\mathbf{kq}} \delta(\varepsilon_{n\mathbf{k}} - \varepsilon_F) \delta(\varepsilon_{m\mathbf{k}+\mathbf{q}} - \varepsilon_F) \lambda_{n\mathbf{k}, m\mathbf{k}+\mathbf{q}}(i\omega_j - i\omega_{j'})}{\sum_{nm} \sum_{\mathbf{kq}} \delta(\varepsilon_{n\mathbf{k}} - \varepsilon_F) \delta(\varepsilon_{m\mathbf{k}+\mathbf{q}} - \varepsilon_F)} \\ &= \int_0^\infty d\omega \frac{2\omega}{(\omega_j - \omega_{j'})^2 + \omega^2} \alpha^2 F(\omega), \end{aligned} \quad (7)$$

where $\alpha^2 F(\omega)$ is the isotropic (double-averaged) Eliashberg spectral function expressed as follows:

$$\begin{aligned}\alpha^2 F(\omega) &= \frac{\sum_{nm} \sum_{\mathbf{kq}} \delta(\varepsilon_{n\mathbf{k}} - \varepsilon_F) \delta(\varepsilon_{m\mathbf{k}+\mathbf{q}} - \varepsilon_F) \alpha^2 F_{n\mathbf{k},m\mathbf{k}+\mathbf{q}}(\omega)}{\sum_{nm} \sum_{\mathbf{kq}} \delta(\varepsilon_{n\mathbf{k}} - \varepsilon_F) \delta(\varepsilon_{m\mathbf{k}+\mathbf{q}} - \varepsilon_F)} \\ &= \frac{1}{N_F} \sum_{nm} \sum_{\mathbf{kq}\nu} \delta(\varepsilon_{n\mathbf{k}} - \varepsilon_F) \delta(\varepsilon_{m\mathbf{k}+\mathbf{q}} - \varepsilon_F) |g_{m\mathbf{k}+\mathbf{q},n\mathbf{k}}^{\mathbf{q}\nu}|^2 \delta(\omega - \omega_{\mathbf{q}\nu}).\end{aligned}\quad (8)$$

We now follow similar steps to define the isotropic average of the non-adiabatic self-energy $\hat{\Sigma}_{n\mathbf{k}}^{(\text{NA})}(i\omega_j)$, as given in Eq. (26) of the main text:

$$\begin{aligned}\hat{\Sigma}^{(\text{NA})}(\varepsilon, i\omega_j) &= \frac{\sum_{n\mathbf{k}} \hat{\Sigma}_{n\mathbf{k}}^{(\text{NA})}(i\omega_j) \delta(\varepsilon_{n\mathbf{k}} - \varepsilon)}{\sum_{n\mathbf{k}} \delta(\varepsilon_{n\mathbf{k}} - \varepsilon)} = \frac{\sum_{n\mathbf{k}} \hat{\Sigma}_{n\mathbf{k}}^{(\text{NA})}(i\omega_j) \delta(\varepsilon_{n\mathbf{k}} - \varepsilon)}{N(\varepsilon)} \\ &= \frac{(k_B T)^2}{N(\varepsilon)} \sum_{n\mathbf{k}} \delta(\varepsilon_{n\mathbf{k}} - \varepsilon) \sum_{mlp} \sum_{\mathbf{qp}} \sum_{j'j''} \frac{\lambda_{n\mathbf{k},m\mathbf{k}+\mathbf{q},l\mathbf{k}+\mathbf{q}+\mathbf{p},p\mathbf{k}+\mathbf{p}}^V(i\omega_j - i\omega_{j'}, i\omega_j - i\omega_{j''})}{N_F^2} \\ &\quad \times \hat{\tau}_3 \hat{G}_{m\mathbf{k}+\mathbf{q}}(i\omega_{j'}) \hat{\tau}_3 \hat{G}_{l\mathbf{k}+\mathbf{q}+\mathbf{p}}(i\omega_{j''} - i\omega_j + i\omega_{j'}) \hat{\tau}_3 \hat{G}_{p\mathbf{k}+\mathbf{p}}(i\omega_{j''}) \hat{\tau}_3.\end{aligned}\quad (9)$$

In the second step, we insert the identities $\int_{-\infty}^{+\infty} d\varepsilon' \delta(\varepsilon_{m\mathbf{k}+\mathbf{q}} - \varepsilon') = 1$, $\int_{-\infty}^{+\infty} d(\varepsilon'' - \varepsilon + \varepsilon') \delta(\varepsilon_{l\mathbf{k}+\mathbf{q}+\mathbf{p}} - (\varepsilon'' - \varepsilon + \varepsilon')) = 1$, and $\int_{-\infty}^{+\infty} d\varepsilon'' \delta(\varepsilon_{p\mathbf{k}+\mathbf{p}} - \varepsilon'') = 1$ into the RHS of Eq. (9) to get

$$\begin{aligned}\hat{\Sigma}^{(\text{NA})}(\varepsilon, i\omega_j) &= \frac{(k_B T)^2}{N(\varepsilon) N_F^2} \sum_{nmlp} \sum_{\mathbf{kqp}} \sum_{j'j''} \delta(\varepsilon_{n\mathbf{k}} - \varepsilon) \int_{-\infty}^{+\infty} d\varepsilon' \delta(\varepsilon_{m\mathbf{k}+\mathbf{q}} - \varepsilon') \int_{-\infty}^{+\infty} d\varepsilon'' \delta(\varepsilon_{p\mathbf{k}+\mathbf{p}} - \varepsilon'') \\ &\quad \times \int_{-\infty}^{+\infty} d(\varepsilon'' - \varepsilon + \varepsilon') \delta(\varepsilon_{l\mathbf{k}+\mathbf{q}+\mathbf{p}} - (\varepsilon'' - \varepsilon + \varepsilon')) \lambda_{n\mathbf{k},m\mathbf{k}+\mathbf{q},l\mathbf{k}+\mathbf{q}+\mathbf{p},p\mathbf{k}+\mathbf{p}}^V(i\omega_j - i\omega_{j'}, i\omega_j - i\omega_{j''}) \\ &\quad \times \hat{\tau}_3 \hat{G}_{m\mathbf{k}+\mathbf{q}}(i\omega_{j'}) \hat{\tau}_3 \hat{G}_{l\mathbf{k}+\mathbf{q}+\mathbf{p}}(i\omega_{j''} - i\omega_j + i\omega_{j'}) \hat{\tau}_3 \hat{G}_{p\mathbf{k}+\mathbf{p}}(i\omega_{j''}) \hat{\tau}_3 \\ &= \frac{(k_B T)^2}{N_F^2} \sum_{j'j''} \int_{-\infty}^{+\infty} d\varepsilon' \int_{-\infty}^{+\infty} d\varepsilon'' \int_{-\infty}^{+\infty} d(\varepsilon'' - \varepsilon + \varepsilon') \frac{N(\varepsilon') N(\varepsilon'') N(\varepsilon'' - \varepsilon + \varepsilon')}{N(\varepsilon) N(\varepsilon') N(\varepsilon'') N(\varepsilon'' - \varepsilon + \varepsilon')} \\ &\quad \times \sum_{nmlp} \sum_{\mathbf{kqp}} \sum_{j'j''} \delta(\varepsilon_{n\mathbf{k}} - \varepsilon) \delta(\varepsilon_{m\mathbf{k}+\mathbf{q}} - \varepsilon') \delta(\varepsilon_{p\mathbf{k}+\mathbf{p}} - \varepsilon'') \delta(\varepsilon_{l\mathbf{k}+\mathbf{q}+\mathbf{p}} - (\varepsilon'' - \varepsilon + \varepsilon')) \\ &\quad \times \lambda_{n\mathbf{k},m\mathbf{k}+\mathbf{q},l\mathbf{k}+\mathbf{q}+\mathbf{p},p\mathbf{k}+\mathbf{p}}^V(i\omega_j - i\omega_{j'}, i\omega_j - i\omega_{j''}) \\ &\quad \times \hat{\tau}_3 \hat{G}_{m\mathbf{k}+\mathbf{q}}(i\omega_{j'}) \hat{\tau}_3 \hat{G}_{l\mathbf{k}+\mathbf{q}+\mathbf{p}}(i\omega_{j''} - i\omega_j + i\omega_{j'}) \hat{\tau}_3 \hat{G}_{p\mathbf{k}+\mathbf{p}}(i\omega_{j''}) \hat{\tau}_3,\end{aligned}\quad (10)$$

where we introduced $\frac{N(\varepsilon') N(\varepsilon'') N(\varepsilon'' - \varepsilon + \varepsilon')}{N(\varepsilon) N(\varepsilon') N(\varepsilon'') N(\varepsilon'' - \varepsilon + \varepsilon')}$ for simplification. As in the adiabatic case, we decouple the integration over the e-ph kernel and the electron Green's function to further simplify the expression. For this purpose, we define the energy-averaged over the RHS of Eq. (10) as follows

$$\begin{aligned}&\frac{1}{N(\varepsilon) N(\varepsilon') N(\varepsilon'') N(\varepsilon'' - \varepsilon + \varepsilon')} \sum_{nmlp} \sum_{\mathbf{kqp}} \sum_{j'j''} \lambda_{n\mathbf{k},m\mathbf{k}+\mathbf{q},l\mathbf{k}+\mathbf{q}+\mathbf{p},p\mathbf{k}+\mathbf{p}}^V(i\omega_j - i\omega_{j'}, i\omega_j - i\omega_{j''}) \\ &\quad \times \delta(\varepsilon_{n\mathbf{k}} - \varepsilon) \delta(\varepsilon_{m\mathbf{k}+\mathbf{q}} - \varepsilon') \delta(\varepsilon_{p\mathbf{k}+\mathbf{p}} - \varepsilon'') \delta(\varepsilon_{l\mathbf{k}+\mathbf{q}+\mathbf{p}} - (\varepsilon'' - \varepsilon + \varepsilon')) \\ &\quad \times \hat{\tau}_3 \hat{G}_{m\mathbf{k}+\mathbf{q}}(i\omega_{j'}) \hat{\tau}_3 \hat{G}_{l\mathbf{k}+\mathbf{q}+\mathbf{p}}(i\omega_{j''} - i\omega_j + i\omega_{j'}) \hat{\tau}_3 \hat{G}_{p\mathbf{k}+\mathbf{p}}(i\omega_{j''}) \hat{\tau}_3 \\ &\approx \lambda^V(\varepsilon, \varepsilon', \varepsilon'', \varepsilon'' - \varepsilon + \varepsilon', i\omega_j - i\omega_{j'}, i\omega_j - i\omega_{j''}) \hat{G}(\varepsilon', i\omega_{j'}) \hat{G}(\varepsilon'' - \varepsilon + \varepsilon', i\omega_{j''} - i\omega_j + i\omega_{j'}) \hat{G}(\varepsilon'', i\omega_{j''}).\end{aligned}\quad (11)$$

As before, we assume that only electronic states close to the Fermi surface contribute to the integral in Eq. (11) (i.e., $\delta(\varepsilon_{n\mathbf{k}} - \varepsilon) \rightarrow \delta(\varepsilon_{n\mathbf{k}} - \varepsilon_F)$, $\delta(\varepsilon_{m\mathbf{k}+\mathbf{q}} - \varepsilon') \rightarrow \delta(\varepsilon_{m\mathbf{k}+\mathbf{q}} - \varepsilon_F)$, $\delta(\varepsilon_{p\mathbf{k}+\mathbf{p}} - \varepsilon'') \rightarrow \delta(\varepsilon_{p\mathbf{k}+\mathbf{p}} - \varepsilon_F)$, and $\delta(\varepsilon_{l\mathbf{k}+\mathbf{q}+\mathbf{p}} - \varepsilon''') \rightarrow \delta(\varepsilon_{l\mathbf{k}+\mathbf{q}+\mathbf{p}} - \varepsilon_F)$) and neglect the energy dependence of the vertex-corrected e-ph kernel λ^V . Thus,

$$\begin{aligned}\lambda^V(\varepsilon, \varepsilon', \varepsilon'', \varepsilon'' - \varepsilon + \varepsilon', i\omega_j - i\omega_{j'}, i\omega_j - i\omega_{j''}) &\approx \lambda^V(\varepsilon_F, \varepsilon_F, \varepsilon_F, \varepsilon_F, i\omega_j - i\omega_{j'}, i\omega_j - i\omega_{j''}) \\ &\equiv \lambda^V(i\omega_j - i\omega_{j'}, i\omega_j - i\omega_{j''}).\end{aligned}\quad (12)$$

Furthermore, as discussed in the adiabatic case, the Green's function depends on $n\mathbf{k}$ only through the band energy $\varepsilon_{n\mathbf{k}}$ (see Eq. (11) in the main text), so the dominant ε dependence of energy-resolved Green's function $\hat{G}(\varepsilon, i\omega_j)$ arises from the explicit appearance of ε (see Sec. IV).

Therefore, the isotropic non-adiabatic self-energy Eq. (10) simplifies to

$$\hat{\Sigma}^{(\text{NA})}(i\omega_j) = \frac{(k_B T)^2}{N_F^2} \sum_{j'j''} \lambda^V(i\omega_j - i\omega_{j'}, i\omega_j - i\omega_{j''}) \int_{-\infty}^{+\infty} d\varepsilon' N(\varepsilon') \int_{-\infty}^{+\infty} d(\varepsilon'' - \varepsilon + \varepsilon') N(\varepsilon'' - \varepsilon + \varepsilon') \int_{-\infty}^{+\infty} d\varepsilon'' N(\varepsilon'') \\ \times \hat{\tau}_3 \hat{G}(\varepsilon', i\omega_{j'}) \hat{\tau}_3 \hat{G}(\varepsilon'' - \varepsilon + \varepsilon', i\omega_{j''} - i\omega_j + i\omega_{j'}) \hat{\tau}_3 \hat{G}(\varepsilon'', i\omega_{j''}) \hat{\tau}_3, \quad (13)$$

where the isotropic vertex corrections to the e-ph kernel $\lambda^V(i\omega_j - i\omega_{j'}, i\omega_j - i\omega_{j''})$ is given by Eq. (32) of the main text.

III. SYMMETRY REDUCTION OF THE VERTEX-CORRECTED ELIASHBERG SPECTRAL FUNCTION

The isotropic vertex-corrected Eliashberg spectral function $\alpha^2 F^V(\omega, \omega')$ is given in Eq. (34) of the main text. We exploit the invariance under the exchange $(\mathbf{q}, \nu, \omega) \leftrightarrow (\mathbf{p}, \mu, \omega')$, which can be understood by examining the corresponding Feynman diagram. The vertex-corrected process, shown in Fig. 1(b) of the main text, involves four electron lines connected by two phonon propagators $D_{\mathbf{q}\nu}^0$ and $D_{\mathbf{p}\mu}^0$. Exchanging the roles of these two phonons in the diagram yields a topologically equivalent physical process, as the electron loop remains closed and the same four electronic states participate in the scattering. This symmetry transformation does not result in a loss of generality due to the complete summation of all phonon modes and electronic states. Under this exchange, the spectral function can be written as:

$$\alpha^2 F^V(\omega, \omega') = \frac{1}{2} \times \frac{1}{C(0)} \sum_{nmlp} \sum_{\mathbf{kqp}} \delta(\varepsilon_{n\mathbf{k}} - \varepsilon_F) \delta(\varepsilon_{m\mathbf{k}+\mathbf{q}} - \varepsilon_F) \delta(\varepsilon_{l\mathbf{k}+\mathbf{q}+\mathbf{p}} - \varepsilon_F) \delta(\varepsilon_{p\mathbf{k}+\mathbf{p}} - \varepsilon_F) \\ \times N_F^2 \sum_{\nu\mu} g_{m\mathbf{k}+\mathbf{q}, n\mathbf{k}}^{\mathbf{q}\nu} g_{l\mathbf{k}+\mathbf{q}+\mathbf{p}, m\mathbf{k}+\mathbf{q}}^{\mathbf{p}\mu} g_{p\mathbf{k}+\mathbf{p}, l\mathbf{k}+\mathbf{q}+\mathbf{p}}^{-\mathbf{q}\nu} g_{n\mathbf{k}, p\mathbf{k}+\mathbf{p}}^{-\mathbf{p}\mu} \delta(\omega - \omega_{\mathbf{q}\nu}) \delta(\omega' - \omega_{\mathbf{p}\mu}) \\ + \frac{1}{2} \times \frac{1}{C(0)} \sum_{nmlp} \sum_{\mathbf{kpq}} \delta(\varepsilon_{n\mathbf{k}} - \varepsilon_F) \delta(\varepsilon_{m\mathbf{k}+\mathbf{p}} - \varepsilon_F) \delta(\varepsilon_{l\mathbf{k}+\mathbf{p}+\mathbf{q}} - \varepsilon_F) \delta(\varepsilon_{p\mathbf{k}+\mathbf{q}} - \varepsilon_F) \\ \times N_F^2 \sum_{\nu\mu} g_{m\mathbf{k}+\mathbf{p}, n\mathbf{k}}^{\mathbf{p}\mu} g_{l\mathbf{k}+\mathbf{p}+\mathbf{q}, m\mathbf{k}+\mathbf{p}}^{\mathbf{q}\nu} g_{p\mathbf{k}+\mathbf{q}, l\mathbf{k}+\mathbf{p}+\mathbf{q}}^{-\mathbf{p}\mu} g_{n\mathbf{k}, p\mathbf{k}+\mathbf{q}}^{-\mathbf{q}\nu} \delta(\omega' - \omega_{\mathbf{p}\mu}) \delta(\omega - \omega_{\mathbf{q}\nu}). \quad (14)$$

Applying the Hermitian property of the e-ph matrix elements, $g_{m\mathbf{k}+\mathbf{q}, n\mathbf{k}}^{\mathbf{q}\nu} = \left[g_{n\mathbf{k}, m\mathbf{k}+\mathbf{q}}^{-\mathbf{q}\nu} \right]^*$, the second term becomes:

$$\frac{1}{2} \times \frac{1}{C(0)} \sum_{nmlp} \sum_{\mathbf{kpq}} \delta(\varepsilon_{n\mathbf{k}} - \varepsilon_F) \delta(\varepsilon_{m\mathbf{k}+\mathbf{p}} - \varepsilon_F) \delta(\varepsilon_{l\mathbf{k}+\mathbf{p}+\mathbf{q}} - \varepsilon_F) \delta(\varepsilon_{p\mathbf{k}+\mathbf{q}} - \varepsilon_F) \\ \times N_F^2 \sum_{\nu\mu} \left[g_{n\mathbf{k}, m\mathbf{k}+\mathbf{p}}^{-\mathbf{p}\mu} \right]^* \left[g_{m\mathbf{k}+\mathbf{p}, l\mathbf{k}+\mathbf{p}+\mathbf{q}}^{-\mathbf{q}\nu} \right]^* \left[g_{l\mathbf{k}+\mathbf{p}+\mathbf{q}, p\mathbf{k}+\mathbf{q}}^{\mathbf{p}\mu} \right]^* \left[g_{p\mathbf{k}+\mathbf{q}, n\mathbf{k}}^{\mathbf{q}\nu} \right]^* \delta(\omega' - \omega_{\mathbf{p}\mu}) \delta(\omega - \omega_{\mathbf{q}\nu}). \quad (15)$$

Since the vertex-corrected spectral function $\alpha^2 F^V(\omega, \omega')$ must be real-valued as it represents a physical observable, we can combine the original term and its complex conjugate to obtain:

$$\alpha^2 F^V(\omega, \omega') = \frac{N_F^2}{C(0)} \sum_{nmlp} \sum_{\mathbf{kqp}} \delta(\varepsilon_{n\mathbf{k}} - \varepsilon_F) \delta(\varepsilon_{m\mathbf{k}+\mathbf{q}} - \varepsilon_F) \delta(\varepsilon_{l\mathbf{k}+\mathbf{q}+\mathbf{p}} - \varepsilon_F) \delta(\varepsilon_{p\mathbf{k}+\mathbf{p}} - \varepsilon_F) \\ \times \text{Re} \left[g_{m\mathbf{k}+\mathbf{q}, n\mathbf{k}}^{\mathbf{q}\nu} g_{l\mathbf{k}+\mathbf{q}+\mathbf{p}, m\mathbf{k}+\mathbf{q}}^{\mathbf{p}\mu} g_{p\mathbf{k}+\mathbf{p}, l\mathbf{k}+\mathbf{q}+\mathbf{p}}^{-\mathbf{q}\nu} g_{n\mathbf{k}, p\mathbf{k}+\mathbf{p}}^{-\mathbf{p}\mu} \right] \delta(\omega - \omega_{\mathbf{q}\nu}) \delta(\omega' - \omega_{\mathbf{p}\mu}). \quad (16)$$

This symmetry-reduced expression allows us to disregard the phase factor in the product of e-ph matrix elements, thereby reducing the computational cost by summing only over identical triplets $(\mathbf{q}, \nu, \omega)$ and $(\mathbf{p}, \mu, \omega')$, and eliminating duplicate contributions without loss of physical content.

IV. SIMPLIFICATION OF THE VERTEX-CORRECTED SELF-ENERGY WITHIN ELIASHBERG FORMALISM

The interacting Green's function $\hat{G}_{n\mathbf{k}}(i\omega_j)$, given in Eq. (11) of the main text, can be written under the isotropic approximation as

$$[\hat{G}(\varepsilon, i\omega_j)]^{-1} = \left[\hat{G}^0(\varepsilon, i\omega_j) \right]^{-1} - \hat{\Sigma}(i\omega_j), \quad (17)$$

where the isotropic non-interacting Green's function $\hat{G}^0(\varepsilon, i\omega_j)$ reduces to

$$\left[\hat{G}^0(\varepsilon, i\omega_j)\right]^{-1} = i\omega_j \hat{\tau}_0 - (\varepsilon - \mu_F) \hat{\tau}_3. \quad (18)$$

Substituting Eq. (18) and the self-energy expression from Eq. (36) of the main text into Eq. (17), we obtain the Dyson equation

$$\left[\hat{G}(\varepsilon, i\omega_j)\right]^{-1} = i\omega_j Z(i\omega_j) \hat{\tau}_0 - [\varepsilon - \mu_F + \chi(i\omega_j)] \hat{\tau}_3 - \phi(i\omega_j) \hat{\tau}_1. \quad (19)$$

Inverting this 2×2 matrix, we get

$$\hat{G}(\varepsilon, i\omega_j) = \frac{i\omega_j Z(i\omega_j) \hat{\tau}_0 + [\varepsilon - \mu_F + \chi(i\omega_j)] \hat{\tau}_3 + \phi(i\omega_j) \hat{\tau}_1}{\det [\hat{G}(\varepsilon, i\omega_j)]^{-1}} = \frac{-i\omega_j Z(i\omega_j) \hat{\tau}_0 - [\varepsilon - \mu_F + \chi(i\omega_j)] \hat{\tau}_3 - \phi(i\omega_j) \hat{\tau}_1}{\Theta(\varepsilon, i\omega_j)}, \quad (20)$$

where

$$\Theta(\varepsilon, i\omega_j) = -\det [\hat{G}(\varepsilon, i\omega_j)]^{-1} = [\omega_j Z(i\omega_j)]^2 + [\varepsilon - \mu_F + \chi(i\omega_j)]^2 + [\phi(i\omega_j)]^2 \quad (21)$$

Using the definitions of $\gamma^Z(\varepsilon, i\omega_j)$, $\gamma^\chi(\varepsilon, i\omega_j)$, and $\gamma^\phi(\varepsilon, i\omega_j)$, as given in Eqs. (46)–(48) of the main text, the Green's function in Eq. (20) reduces to

$$\hat{G}(\varepsilon, i\omega_j) = - \left[i\gamma^Z(\varepsilon, i\omega_j) \hat{\tau}_0 + \gamma^\chi(\varepsilon, i\omega_j) \hat{\tau}_3 + \gamma^\phi(\varepsilon, i\omega_j) \hat{\tau}_1 \right]. \quad (22)$$

To simplify the product $\hat{\tau}_3 \hat{G}(\varepsilon, i\omega_j) \hat{\tau}_3$ in Eq. (22), we use

$$\hat{\tau}_3 \hat{G}(\varepsilon, i\omega_j) \hat{\tau}_3 = -\hat{\tau}_3 \left[i\gamma^Z(\varepsilon, i\omega_j) \hat{\tau}_0 + \gamma^\chi(\varepsilon, i\omega_j) \hat{\tau}_3 + \gamma^\phi(\varepsilon, i\omega_j) \hat{\tau}_1 \right] \hat{\tau}_3 = (-1) \left[i\gamma^Z(\varepsilon, i\omega_j) \hat{\tau}_0 + \gamma^\chi(\varepsilon, i\omega_j) \hat{\tau}_3 - \gamma^\phi(\varepsilon, i\omega_j) \hat{\tau}_1 \right]. \quad (23)$$

The Pauli matrices obey the identity,

$$\hat{\tau}_i \hat{\tau}_j = i\epsilon_{ijk} \hat{\tau}_k + \delta_{ij} \hat{\tau}_0, \quad (24)$$

where ϵ_{ijk} is the Levi-Civita symbol, as illustrated in Fig. S2.

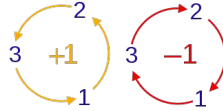


FIG. S2. ϵ_{ijk} is +1 for cyclic permutations of (1, 2, 3) (left), -1 for anti-cyclic permutations (right) and 0 otherwise.

Using these algebraic relations, we simplify the triple product of Green's functions in Eq. (31) of the main text:

$$-\hat{\tau}_3 \hat{G}(\varepsilon', i\omega_j) \hat{\tau}_3 \hat{G}(\varepsilon'' - \varepsilon + \varepsilon', i\omega_{j''} - i\omega_j + i\omega_{j'}) \hat{\tau}_3 \hat{G}(\varepsilon'', i\omega_{j''}) \hat{\tau}_3 = a_0 \hat{\tau}_0 + a_1 \hat{\tau}_1 + a_2 \hat{\tau}_3, \quad (25)$$

where the coefficients a_0 , a_1 , and a_2 are given by

$$a_0 = -i\gamma_1^Z \gamma_2^Z \gamma_3^Z + i\gamma_1^Z \gamma_2^X \gamma_3^X - i\gamma_1^Z \gamma_2^\phi \gamma_3^\phi + i\gamma_1^X \gamma_2^Z \gamma_3^X + i\gamma_1^X \gamma_2^X \gamma_3^Z + i\gamma_1^\phi \gamma_2^Z \gamma_3^\phi - i\gamma_1^\phi \gamma_2^\phi \gamma_3^Z, \quad (26a)$$

$$a_1 = \gamma_1^Z \gamma_2^Z \gamma_3^\phi - \gamma_1^Z \gamma_2^\phi \gamma_3^Z - \gamma_1^X \gamma_2^X \gamma_3^\phi - \gamma_1^X \gamma_2^\phi \gamma_3^X + \gamma_1^\phi \gamma_2^Z \gamma_3^Z - \gamma_1^\phi \gamma_2^X \gamma_3^X + \gamma_1^\phi \gamma_2^\phi \gamma_3^\phi, \quad (26b)$$

$$a_2 = -\gamma_1^Z \gamma_2^Z \gamma_3^X - \gamma_1^Z \gamma_2^X \gamma_3^Z - \gamma_1^X \gamma_2^Z \gamma_3^Z + \gamma_1^X \gamma_2^X \gamma_3^X - \gamma_1^\phi \gamma_2^X \gamma_3^\phi - \gamma_1^\phi \gamma_2^\phi \gamma_3^X. \quad (26c)$$

Here, for brevity, we define $\gamma_1^{Z/X/\phi} \equiv \gamma_1^{Z/X/\phi}(\varepsilon', i\omega_{j'})$, $\gamma_2^{Z/X/\phi} \equiv \gamma_2^{Z/X/\phi}(\varepsilon'' - \varepsilon + \varepsilon', i\omega_{j''} - i\omega_j + i\omega_{j'})$, and $\gamma_3^{Z/X/\phi} \equiv \gamma_3^{Z/X/\phi}(\varepsilon'', i\omega_{j''})$. Finally, we note that the $\hat{\tau}_2$ component is neglected because the functions $\phi(\varepsilon, i\omega_j)$ and $\bar{\phi}(\varepsilon, i\omega_j)$ are proportional within an arbitrary phase. Without loss of generality, we set the relative phase such that $\bar{\phi}(\varepsilon, i\omega_j) = 0$ [2, 4, 6, 7].

Following the standard Eliashberg procedure, we equate the coefficients of $\hat{\tau}_0$, $\hat{\tau}_3$, and $\hat{\tau}_1$ in the self-energy expressions (Eqs. (6) and (13)) to obtain the self-consistent Eliashberg equations for $Z(i\omega_j)$, $\chi(i\omega_j)$, and $\phi(i\omega_j)$, which are given in Eqs. (37)–(39) of the main text.

V. SUMMATION PROCEDURE OVER MATSUBARA FREQUENCIES

In the imaginary-time formalism of finite-temperature quantum field theory, Matsubara frequencies arise from the Fourier transformation of time-dependent correlation functions. For fermions, the Matsubara frequencies are given by

$$i\omega_j = i(2j+1)\pi k_B T \quad (27)$$

where j is an integer and T is the temperature. For bosons, the corresponding Matsubara frequencies are even as given by the formula

$$i\tilde{\omega}_l = i(2l)\pi k_B T \quad (28)$$

The self-energy expressions involve summations over fermionic and bosonic Matsubara frequencies associated with electronic and phononic Green's functions, respectively. In practical calculations, these infinite sums are truncated by introducing a cutoff frequency ω_c , typically chosen to be ten times the maximum phonon frequency to ensure convergence of the Eliashberg equations.

The fermionic Matsubara summation is performed over the range $j \in [-N_c - 1, N_c]$, where the cutoff index N_c is defined as

$$\begin{aligned} \omega_{j_{max}} \leq \omega_c &\implies (2j_{max} + 1)\pi k_B T \leq \omega_c \\ &\implies j_{max} = \text{INT} \left[\frac{1}{2} \left(\frac{\omega_c}{\pi k_B T} - 1 \right) \right] \equiv N_c \end{aligned} \quad (29)$$

Owing to the even symmetry of the phonon propagator $D_{\mathbf{q}\nu}(i\tilde{\omega}_l) = 2\omega_{\mathbf{q}\nu}/[(i\tilde{\omega}_l)^2 - \omega_{\mathbf{q}\nu}^2]$ and the resulting structure of the Eliashberg equations, the self-energy components $Z(i\omega_j)$, $\chi(i\omega_j)$, and $\phi(i\omega_j)$ are even functions of the Matsubara index j . This allows for efficient summation by exploiting the identity $\omega_{-j} = -\omega_{j-1}$ and regrouping terms with appropriate sign conventions.

As an example, we demonstrate this procedure for the adiabatic contribution to the mass renormalization function $Z^{(A)}(i\omega_j)$ from Eq. (37) of the main text. The expression reads:

$$Z^{(A)}(i\omega_j) = 1 + \frac{k_B T}{\omega_j N_F} \sum_{j'=-N_c+1}^{N_c} \lambda(i\omega_j - i\omega_{j'}) \int_{-\infty}^{\infty} d\varepsilon' N(\varepsilon') \gamma^Z(\varepsilon', i\omega_{j'}). \quad (30)$$

Splitting the sum into negative and non-negative components, we get

$$\begin{aligned} Z^{(A)}(i\omega_j) = 1 + \frac{k_B T}{\omega_j N_F} &\left[\sum_{j'=-N_c+1}^{-1} \lambda(i\omega_j - i\omega_{j'}) \int_{-\infty}^{\infty} d\varepsilon' N(\varepsilon') \gamma^Z(\varepsilon', i\omega_{j'}) \right. \\ &\left. + \sum_{j'=0}^{N_c} \lambda(i\omega_j - i\omega_{j'}) \int_{-\infty}^{\infty} d\varepsilon' N(\varepsilon') \gamma^Z(\varepsilon', i\omega_{j'}) \right]. \end{aligned} \quad (31)$$

For the negative indices ($j' < 0$), substituting $j' \rightarrow -j' - 1$ maps the sum over $j' \in [-N_c - 1, -1]$ to $j' \in [0, N_c]$:

$$\begin{aligned} Z^{(A)}(i\omega_j) &= 1 + \frac{k_B T}{\omega_j N_F} \sum_{j'=0}^{N_c} \left[\lambda(i\omega_j + i\omega_{j'}) \int d\varepsilon' N(\varepsilon') \gamma^Z(\varepsilon', -i\omega_{j'}) + \lambda(i\omega_j - i\omega_{j'}) \int d\varepsilon' N(\varepsilon') \gamma^Z(\varepsilon', i\omega_{j'}) \right] \\ &= 1 + \frac{k_B T}{\omega_j N_F} \sum_{j'=0}^{N_c} [\lambda(i\omega_j - i\omega_{j'}) - \lambda(i\omega_j + i\omega_{j'})] \int d\varepsilon' N(\varepsilon') \gamma^Z(\varepsilon', i\omega_{j'}). \end{aligned} \quad (32)$$

A similar approach can be applied to the Matsubara summations for other quantities, including $\phi^{(A)}(i\omega_j)$, $\chi^{(A)}(i\omega_j)$, N_e and the terms corresponding to the non-adiabatic vertex corrections. This transformation ensures that all summations are evaluated over positive Matsubara frequencies only, thereby simplifying the numerical implementation.

VI. DERIVATION OF THE ISOTROPIC FERMI-SURFACE RESTRICTED EXPRESSIONS

We further simplify the isotropic Eliashberg equations by assuming the constant density of states, i.e., $N(\varepsilon') \rightarrow N_F$. Under this assumption, the adiabatic self-energy in Eq. (6) becomes

$$\begin{aligned}\hat{\Sigma}^{(A)}(i\omega_j) &= k_B T \sum_{j'} \frac{\lambda(i\omega_j - i\omega_{j'})}{N_F} N_F \int_{-\infty}^{\infty} d\varepsilon' \hat{\tau}_3 \hat{G}(\varepsilon', i\omega_{j'}) \hat{\tau}_3 \\ &= -k_B T \sum_{j'} \int_{-\infty}^{\infty} d\varepsilon' \frac{i\omega_{j'} Z(i\omega_{j'}) \hat{\tau}_0 + [\varepsilon' - \mu_F + \chi(i\omega_{j'})] \hat{\tau}_3 - \phi(i\omega_{j'}) \hat{\tau}_1}{[\omega_{j'} Z(i\omega_{j'})]^2 + [\varepsilon' - \mu_F + \chi(i\omega_{j'})]^2 + [\phi(i\omega_{j'})]^2}.\end{aligned}\quad (33)$$

We now perform the integral over ε' analytically. The poles of the Green's function are given by:

$$\varepsilon' - \mu_F + \chi(i\omega_{j'}) = \pm i \sqrt{[\omega_{j'} Z(i\omega_{j'})]^2 + [\phi(i\omega_{j'})]^2}.\quad (34)$$

Using the contour integration identity $\int_{-\infty}^{\infty} \frac{dx}{x^2 + a^2} = \frac{\pi}{a}$ and noting that the integrand term involving $(\varepsilon' - \mu_F + \chi)$ is odd in ε' in the upper-half plane, the relevant integrals reduce to:

$$\begin{aligned}& \int d\varepsilon' \frac{1}{[\omega_{j'} Z(i\omega_{j'})]^2 + [\varepsilon' - \mu_F + \chi(i\omega_{j'})]^2 + [\phi(i\omega_{j'})]^2} \times \left\{ \varepsilon' - \mu_F + \chi(i\omega_{j'}) \right\} \\ &= \left\{ \frac{\pi}{\sqrt{[\omega_{j'} Z(i\omega_{j'})]^2 + [\phi(i\omega_{j'})]^2}} = \bar{\Theta}(i\omega_{j'}) \right\}, \\ & \quad 0 \text{ (odd in } \varepsilon')\end{aligned}\quad (35)$$

where we define

$$\bar{\Theta}(i\omega_{j'}) = \sqrt{[\omega_{j'} Z(i\omega_{j'})]^2 + [\phi(i\omega_{j'})]^2},\quad (36a)$$

$$\tilde{\gamma}^Z(i\omega_{j'}) = \frac{\omega_{j'} Z(i\omega_{j'})}{\bar{\Theta}(i\omega_{j'})}, \quad \tilde{\gamma}^\phi(i\omega_{j'}) = \frac{\phi(i\omega_{j'})}{\bar{\Theta}(i\omega_{j'})}.\quad (36b)$$

Substituting these results into Eq. (33), the adiabatic self-energy under the FSR limit simplifies to

$$\hat{\Sigma}^{(A)}(i\omega_j) = -\pi k_B T \sum_{j'} \lambda(i\omega_j - i\omega_{j'}) \left[i\tilde{\gamma}^Z(i\omega_{j'}) \hat{\tau}_0 - \tilde{\gamma}^\phi(i\omega_{j'}) \hat{\tau}_1 \right].\quad (37)$$

We now turn to the non-adiabatic self-energy in Eq. (13), again assuming $N(\varepsilon') \rightarrow N_F$, $N(\varepsilon'') \rightarrow N_F$, and $N(\varepsilon'' - \varepsilon + \varepsilon') \rightarrow N_F$, with μ_F constant, the expression becomes

$$\begin{aligned}\hat{\Sigma}^{(NA)}(i\omega_j) &= (k_B T)^2 N_F \sum_{j'j''} \lambda^V(i\omega_j - i\omega_{j'}, i\omega_j - i\omega_{j''}) \\ &\quad \times \int_{-\infty}^{\infty} d\varepsilon' \int_{-\infty}^{\infty} d(\varepsilon'' - \varepsilon + \varepsilon') \int_{-\infty}^{\infty} d\varepsilon'' \hat{\tau}_3 \hat{G}(\varepsilon', i\omega_{j'}) \hat{\tau}_3 \hat{G}(\varepsilon'' - \varepsilon + \varepsilon', i\omega_{j''} - i\omega_j + i\omega_{j'}) \hat{\tau}_3 \hat{G}(\varepsilon'', i\omega_{j''}) \hat{\tau}_3.\end{aligned}\quad (38)$$

Performing the analytical integrals over ε' , ε'' , and $\varepsilon'' - \varepsilon + \varepsilon'$ in Eq. (38), the χ term vanishes since it is an odd function in energy. The integrand is solved using a similar approach as described in Eq. (35), yielding

$$\begin{aligned}\hat{\Sigma}^{(NA)}(i\omega_j) &= -\pi^3 (k_B T)^2 N_F \sum_{j'j''} \lambda^V(i\omega_j - i\omega_{j'}, i\omega_j - i\omega_{j''}) \\ &\quad \times \left[-i\tilde{\gamma}^Z(i\omega_{j'}) \tilde{\gamma}^Z(i\omega_{j''} - i\omega_j + i\omega_{j'}) \tilde{\gamma}^Z(i\omega_{j''}) \hat{\tau}_0 + \tilde{\gamma}^Z(i\omega_{j'}) \tilde{\gamma}^Z(i\omega_{j''} - i\omega_j + i\omega_{j'}) \tilde{\gamma}^\phi(i\omega_{j''}) \hat{\tau}_1 \right. \\ &\quad - \tilde{\gamma}^Z(i\omega_{j'}) \tilde{\gamma}^\phi(i\omega_{j''} - i\omega_j + i\omega_{j'}) \tilde{\gamma}^Z(i\omega_{j''}) \hat{\tau}_1 - i\tilde{\gamma}^Z(i\omega_{j'}) \tilde{\gamma}^\phi(i\omega_{j''} - i\omega_j + i\omega_{j'}) \tilde{\gamma}^\phi(i\omega_{j''}) \hat{\tau}_0 \\ &\quad + \tilde{\gamma}^\phi(i\omega_{j'}) \tilde{\gamma}^Z(i\omega_{j''} - i\omega_j + i\omega_{j'}) \tilde{\gamma}^Z(i\omega_{j''}) \hat{\tau}_1 + i\tilde{\gamma}^\phi(i\omega_{j'}) \tilde{\gamma}^Z(i\omega_{j''} - i\omega_j + i\omega_{j'}) \tilde{\gamma}^\phi(i\omega_{j''}) \hat{\tau}_0 \\ &\quad \left. - i\tilde{\gamma}^\phi(i\omega_{j'}) \tilde{\gamma}^\phi(i\omega_{j''} - i\omega_j + i\omega_{j'}) \tilde{\gamma}^Z(i\omega_{j''}) \hat{\tau}_0 + \tilde{\gamma}^\phi(i\omega_{j'}) \tilde{\gamma}^\phi(i\omega_{j''} - i\omega_j + i\omega_{j'}) \tilde{\gamma}^\phi(i\omega_{j''}) \hat{\tau}_1 \right].\end{aligned}\quad (39)$$

Thus, the total self-energy within the isotropic FSR approximation is the sum of the adiabatic term in Eq. (37) and the non-adiabatic term in Eq. (39). Following the standard procedure, we match the coefficients of $\hat{\tau}_0$ and $\hat{\tau}_1$ in the total self-energy. Equating $\hat{\tau}_0$ terms, we obtain the expression for $Z(i\omega_j)$:

$$\begin{aligned}
Z(i\omega_j) &= 1 + \frac{\pi k_B T}{\omega_j} \sum_{j'} \lambda(i\omega_j - i\omega_{j'}) \tilde{\gamma}^Z(i\omega_{j'}) \\
&\quad + \frac{\pi^3 (k_B T)^2 N_F}{\omega_j} \sum_{j'j''} \lambda^V(i\omega_j - i\omega_{j'}, i\omega_j - i\omega_{j''}) \\
&\quad \times \left[-\tilde{\gamma}^Z(i\omega_{j'}) \tilde{\gamma}^Z(i\omega_{j''} - i\omega_j + i\omega_{j'}) \tilde{\gamma}^Z(i\omega_{j''}) - \tilde{\gamma}^Z(i\omega_{j'}) \tilde{\gamma}^\phi(i\omega_{j''} - i\omega_j + i\omega_{j'}) \tilde{\gamma}^\phi(i\omega_{j''}) \right. \\
&\quad \left. + \tilde{\gamma}^\phi(i\omega_{j'}) \tilde{\gamma}^Z(i\omega_{j''} - i\omega_j + i\omega_{j'}) \tilde{\gamma}^\phi(i\omega_{j''}) - \tilde{\gamma}^\phi(i\omega_{j'}) \tilde{\gamma}^\phi(i\omega_{j''} - i\omega_j + i\omega_{j'}) \tilde{\gamma}^Z(i\omega_{j''}) \right] \\
&= 1 + \frac{\pi k_B T}{\omega_j} \sum_{j'} \lambda(i\omega_j - i\omega_{j'}) \tilde{\gamma}^Z(i\omega_{j'}) \\
&\quad + \frac{\pi^3 (k_B T)^2 N_F}{\omega_j} \sum_{j'j''} \lambda^V(i\omega_j - i\omega_{j'}, i\omega_j - i\omega_{j''}) \left[\tilde{\gamma}^T(i\omega_{j'}) \tilde{P}^Z(i\omega_{j''} - i\omega_j + i\omega_{j'}) \tilde{\gamma}(i\omega_{j''}) \right]. \tag{40}
\end{aligned}$$

Similarly, matching $\hat{\tau}_1$ coefficients gives the expression for $\phi(i\omega_j)$:

$$\begin{aligned}
\phi(i\omega_j) &= \pi k_B T \sum_{j'} \lambda(i\omega_j - i\omega_{j'}) \tilde{\gamma}^\phi(i\omega_{j'}) \\
&\quad + \pi^3 (k_B T)^2 N_F \sum_{j'j''} \lambda^V(i\omega_j - i\omega_{j'}, i\omega_j - i\omega_{j''}) \\
&\quad \times \left[-\tilde{\gamma}^Z(i\omega_{j'}) \tilde{\gamma}^Z(i\omega_{j''} - i\omega_j + i\omega_{j'}) \tilde{\gamma}^\phi(i\omega_{j''}) + \tilde{\gamma}^Z(i\omega_{j'}) \tilde{\gamma}^\phi(i\omega_{j''} - i\omega_j + i\omega_{j'}) \tilde{\gamma}^Z(i\omega_{j''}) \right. \\
&\quad \left. - \tilde{\gamma}^\phi(i\omega_{j'}) \tilde{\gamma}^Z(i\omega_{j''} - i\omega_j + i\omega_{j'}) \tilde{\gamma}^Z(i\omega_{j''}) - \tilde{\gamma}^\phi(i\omega_{j'}) \tilde{\gamma}^\phi(i\omega_{j''} - i\omega_j + i\omega_{j'}) \tilde{\gamma}^\phi(i\omega_{j''}) \right] \tag{41} \\
&= \pi k_B T \sum_{j'} \lambda(i\omega_j - i\omega_{j'}) \tilde{\gamma}^\phi(i\omega_{j'}) \\
&\quad + \pi^3 (k_B T)^2 N_F \sum_{j'j''} \lambda^V(i\omega_j - i\omega_{j'}, i\omega_j - i\omega_{j''}) \left[\tilde{\gamma}^T(i\omega_{j'}) \tilde{P}^\phi(i\omega_{j''} - i\omega_j + i\omega_{j'}) \tilde{\gamma}(i\omega_{j''}) \right], \tag{42}
\end{aligned}$$

where $\tilde{\gamma}$, \tilde{P}^Z and \tilde{P}^ϕ expressions are given by Eqs. (52)–(54) in the main text.

VII. CONVERGENCE OF HARMONIC AND ANHARMONIC PHONON CALCULATIONS FOR H₃S

In order to achieve convergence of the harmonic phonons for H₃S at 200 GPa, we varied the \mathbf{q} -mesh and computed the phonon dispersions shown in Fig. S3(a). It indicates high sensitivity to the \mathbf{q} -point meshes. For instance, a $3 \times 3 \times 3$ \mathbf{q} -grid results in the emergence of imaginary modes, highlighting the necessity of incorporating anharmonic effects to accurately describe the phonon properties of H₃S [8, 9]. Further Fig. S3(b) shows the convergence of phonon dispersion with respect to the kinetic energy cutoff, indicating that a cutoff of 60 Ry is sufficient in this system.

We employed the special displacement method implemented in the ZG code [10, 11] to compute phonons with anharmonic corrections. Since these calculations become increasingly expensive with larger supercell sizes, we assessed the phonon convergence using a $2 \times 2 \times 2$ supercell with \mathbf{k} -meshes of $12 \times 12 \times 12$ and $24 \times 24 \times 24$. The close agreement between the results shown in Fig. S4(a) indicates that the coarser $12 \times 12 \times 12$ mesh is sufficient for accurately computing interatomic force constants (IFCs) in the special displacement framework, and is thus adopted in our anharmonic phonon calculations. We also examined the convergence of anharmonic phonon spectra with respect to the magnitude of atomic displacements within a $2 \times 2 \times 2$ supercell. As shown in Fig. S4(b), a displacement amplitude of 0.01 Å yields converged results and is therefore adopted in this study. Larger displacements lead to unphysical shifts in the optical phonon branches associated with hydrogen vibrations.

Finally, we examined the convergence of anharmonic phonon frequencies using $2 \times 2 \times 2$, $3 \times 3 \times 3$, and $4 \times 4 \times 4$ supercells. As shown in Fig. S5(a), all three supercell sizes yield closely matching results in the low- and mid-frequency ranges. However, the $4 \times 4 \times 4$ supercell better resolves fine features in the high-frequency region, particularly those associated with hydrogen vibrations. For improved accuracy, we therefore adopted the $4 \times 4 \times 4$ supercell in all subsequent

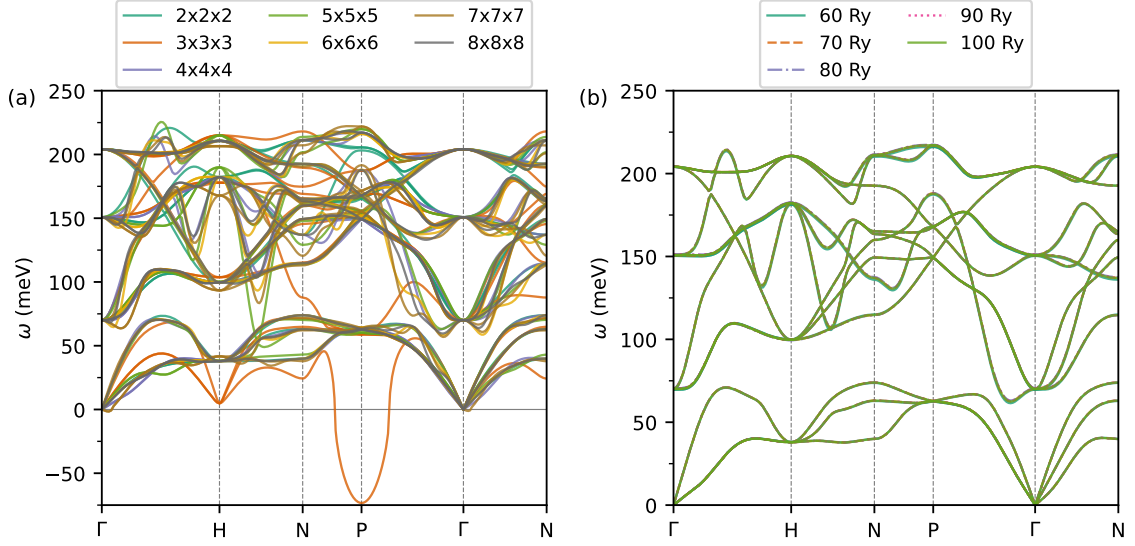


FIG. S3. (a) Convergence of the harmonic phonon dispersion of H₃S at 200 GPa with respect to the \mathbf{q} -point sampling, ranging from $2 \times 2 \times 2$ to $8 \times 8 \times 8$. Notably, imaginary modes appear when using a $3 \times 3 \times 3$ \mathbf{q} -grid, which are eliminated when anharmonic corrections are included. (b) Convergence of harmonic phonon dispersion with respect to the kinetic energy cutoff, ranging from 60 Ry to 100 Ry. A cutoff of 60 Ry is found to be sufficient for accurate phonon calculations.

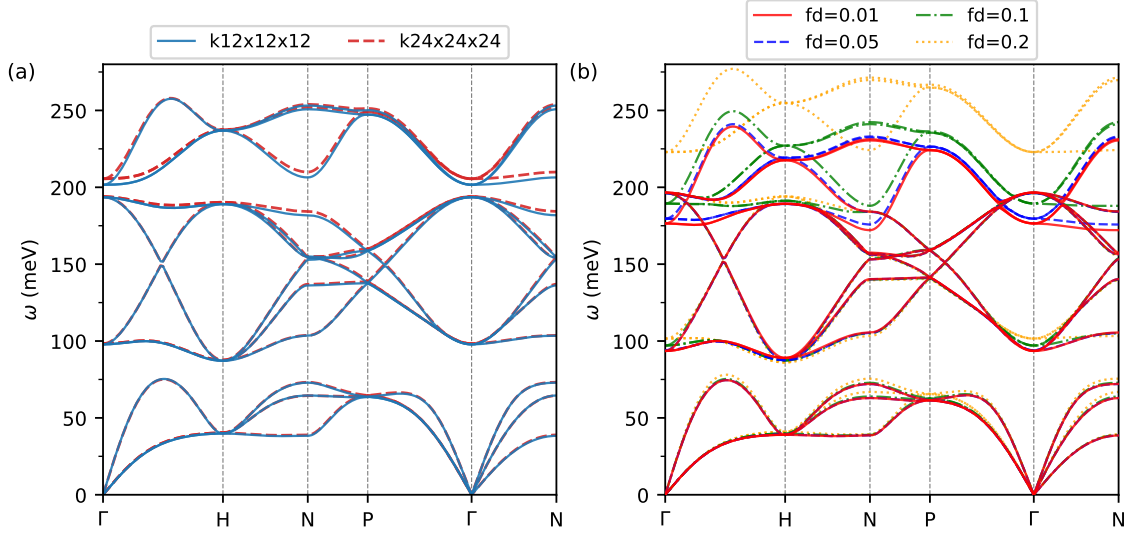


FIG. S4. (a) Comparison of anharmonic phonon dispersion of H₃S at 200 GPa using the IFCs from the first ZG iteration, computed with a $2 \times 2 \times 2$ supercell and \mathbf{k} -meshes of $12 \times 12 \times 12$ (blue solid line) and $24 \times 24 \times 24$ (red dashed line). (b) Anharmonic phonon dispersion computed using finite displacement amplitudes ranging from 0.01 Å to 0.2 Å. At large displacements (e.g., 0.2 Å), the two highest frequency optical phonon branches are separated from the rest, signaling an unphysical behavior. A displacement of 0.01 Å yields converged and physically meaningful results, and is adopted throughout this study.

anharmonic calculations. Using a linear mixing scheme within the ZG framework, the anharmonic spectrum for H₃S typically converged within 4–5 iterations, as illustrated in Fig. S5(b).

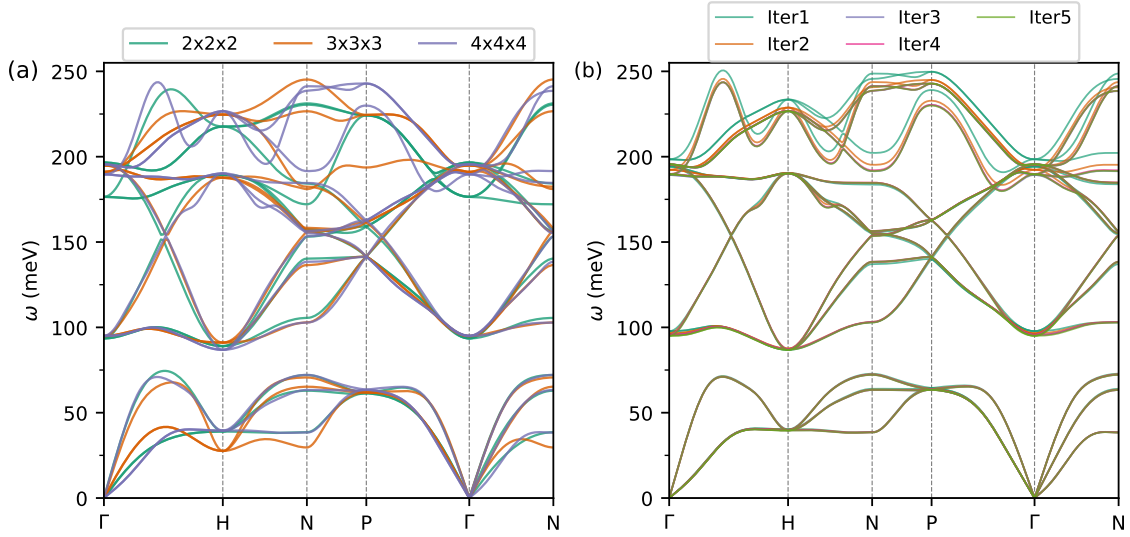


FIG. S5. (a) Convergence of anharmonic phonon spectra of H_3S at 200 GPa with respect to supercell size, ranging from $2 \times 2 \times 2$ to $4 \times 4 \times 4$. (b) Convergence of the anharmonic phonon spectrum as a function of the number of iterations in the ZG scheme using a linear mixing scheme. IFCs at each iteration were evaluated by finite differences with atomic displacements of 0.01 Å.

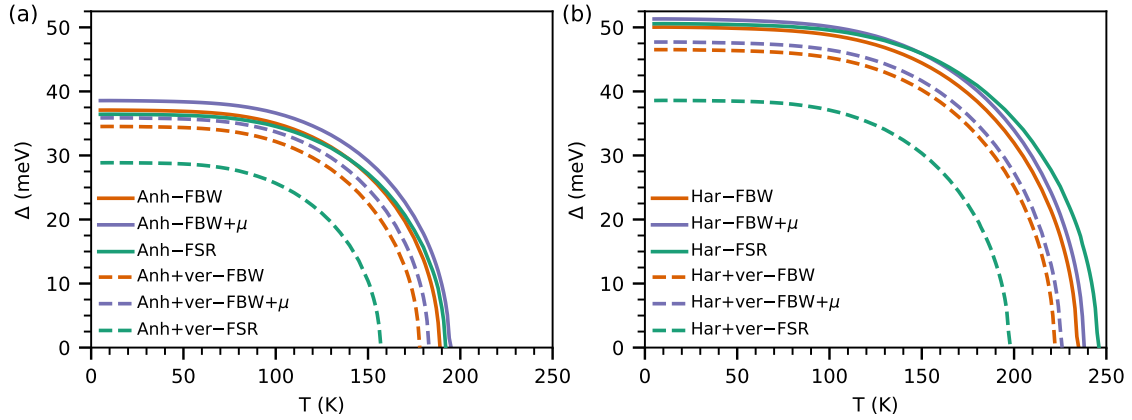


FIG. S6. The isotropic superconducting gap $\Delta(T)$ for H_3S at 200 GPa computed using various levels of theoretical approaches with an effective Coulomb parameter $\mu_{\text{E}}^* = 0.16$ for (a) anharmonic phonons, and (b) harmonic phonons. Solid lines denote adiabatic calculations (FBW: orange, FBW+ μ : purple, and FSR: teal-green), while dashed lines include vertex corrections (ver-FBW: dashed orange, ver-FBW+ μ : dashed purple, and ver-FSR: dashed teal-green).

VIII. SUPERCONDUCTING PROPERTIES WITH VERTEX CORRECTIONS FOR H_3S

Figure S6(a) shows the isotropic superconducting gap $\Delta(T)$ for H_3S computed using the FSR, FBW, and FBW+ μ methods with anharmonic phonons, both with (dashed lines) and without vertex corrections (solid lines). In the adiabatic FSR approach, we obtain a critical temperature $T_c \approx 192$ K, slightly higher than the values obtained with FBW (189 K) and FBW+ μ (195 K), due to the omission of the energy dependence of the electronic density of states (DOS). When vertex corrections are included within the FSR framework, T_c is significantly reduced by approximately 35 K, yielding a value that falls well below the experimental range of 175–185 K [12]. By contrast, including vertex corrections within the FBW and FBW+ μ schemes leads to a more moderate 10 K reduction in T_c , resulting in predictions that closely match experimental measurements.

To understand the origin of the difference in T_c between the FSR and FBW methods, both with and without vertex corrections, it is useful to examine how DOS enters into each formulation. In the adiabatic limit, the FSR expressions (first line in Eqs. (50) and (51) of the main text) do not explicitly depend on N_{F} , whereas the FBW expressions

TABLE S1. Zero-temperature superconducting gap $\Delta(0)$, critical temperature T_c , and BCS ratio $2\Delta(0)/k_B T_c$ computed using the adiabatic (FBW, FBW+ μ , and FSR) and vertex-corrected (ver-FBW, ver-FBW+ μ , and ver-FSR) approaches with harmonic and anharmonic phonons. A Coulomb pseudopotential of $\mu_E^* = 0.16$ is used. Other theoretical studies include FSR results from Errea *et al.* [8], obtained using both harmonic and anharmonic phonons, and average values from the anisotropic FBW and FBW+ μ results of Lucrezi *et al.* [7].

Phonons	Method	Present work			Other theoretical studies		
		$\Delta(0)$ (meV)	T_c (K)	$2\Delta(0)/k_B T_c$	$\Delta(0)$ (meV)	T_c (K)	$2\Delta(0)/k_B T_c$
Anharmonic	FSR	36.43	192	4.40	36.6	194	4.38
	FBW	37.08	189	4.55			
	FBW+ μ	38.56	195	4.59			
Anharmonic	ver-FSR	28.85	157	4.27			
	ver-FBW	34.52	178	4.50			
	ver-FBW+ μ	35.86	183	4.55			
Harmonic	FSR	50.57	246	4.77	53.0	250	4.92
	FBW	50.04	235	4.94	54.4	250	5.05
	FBW+ μ	51.31	238	5.00	50.0	232	5.00
Harmonic	ver-FSR	38.58	198	4.52			
	ver-FBW	46.52	222	4.86			
	ver-FBW+ μ	47.71	226	4.90			

(first line in Eqs. (37)–(39) of the main text) include N_F in the denominator and integrate over the energy-dependent electronic DOS, thereby capturing its full variation around the Fermi level ε_F . For H_3S , which features a prominent van Hove singularity near ε_F with $N_F \approx 0.32$ states/eV/spin/cell, this leads to a slightly lower T_c in FBW compared to FSR. In the non-adiabatic regime, vertex corrections further modify the DOS dependence. In the ver-FSR formulation, N_F enters explicitly in the numerator (second line in Eqs. (50) and (51) of the main text), amplifying the impact of a peaked DOS at ε_F . In contrast, the ver-FBW formulation includes N_F^2 in the denominator and performs a threefold integration over the energy-resolved DOS (second line in Eqs. (37)–(39) of the main text), thereby capturing the detailed DOS variation near ε_F .

Figure S6(b) presents results analogous to those in Fig. S6(a), but using harmonic phonons. Consistent with previous studies [8, 13], we find that harmonic phonons significantly overestimate the T_c across all three methods. When vertex corrections are included in the FSR approach, T_c is reduced by 48 K, an even larger suppression than that observed in the anharmonic case. In contrast, incorporating the energy dependence of the DOS within the FBW framework yields a more moderate reduction in T_c , on the order of 12–13 K, comparable to that found with anharmonic phonons. Table S1 summarizes the zero-temperature superconducting gap $\Delta(0)$, critical temperature T_c , and BCS ratio $2\Delta(0)/k_B T_c$ computed in this study within the adiabatic and non-adiabatic formalisms, using harmonic and anharmonic phonons. These results are compared against previous theoretical predictions based on the Eliashberg formalism [7, 8] and recent experimental measurements [14].

* mshashi125@gmail.com

† rmargine@binghamton.edu

- [1] A. B. Migdal, *Sov. Phys. JETP* **7**, 996 (1958).
- [2] P. B. Allen and B. Mitrović (Academic Press, 1983) pp. 1–92.
- [3] R. Heid, Lecture Notes of the Autumn School on Correlated Electrons; Pavarini, E., Koch, E., Scalettar, R., Martin, R., Eds., 399 (2017).
- [4] F. Schrodi, P. M. Oppeneer, and A. Aperis, *Phys. Rev. B* **102**, 024503 (2020).
- [5] W. E. Pickett, *Phys. Rev. B* **26**, 1186 (1982).
- [6] S. Poncé, E. Margine, C. Verdi, and F. Giustino, *Comput. Phys. Commun.* **209**, 116 (2016).
- [7] R. Lucrezi, P. P. Ferreira, S. Hajinazar, H. Mori, H. Paudyal, E. R. Margine, and C. Heil, *Commun. Phys.* **7**, 33 (2024).
- [8] I. Errea, M. Calandra, C. J. Pickard, J. Nelson, R. J. Needs, Y. Li, H. Liu, Y. Zhang, Y. Ma, and F. Mauri, *Phys. Rev. Lett.* **114**, 157004 (2015).
- [9] R. Taureau, M. Cherubini, T. Morresi, and M. Casula, *npj Comput. Mater.* **10**, 56 (2024).
- [10] M. Zacharias and F. Giustino, *Phys. Rev. Res.* **2** (2020).

- [11] M. Zacharias, G. Volonakis, F. Giustino, and J. Even, [Phys. Rev. B **108**, 035155 \(2023\)](#).
- [12] A. P. Drozdov, M. I. Erements, I. A. Troyan, V. Ksenofontov, and S. I. Shylin, [Nature **525**, 73 \(2015\)](#).
- [13] W. Sano, T. Koretsune, T. Tadano, R. Akashi, and R. Arita, [Phys. Rev. B **93**, 094525 \(2016\)](#).
- [14] F. Du, A. P. Drozdov, V. S. Minkov, F. F. Balakirev, P. Kong, G. A. Smith, J. Yan, B. Shen, P. Gegenwart, and M. I. Erements, [Nature **641**, 619–624 \(2025\)](#).